Cation Effects on the Brønsted Acidity of Solid Tungstosilicic Acid Clusters

Guangming Cai,^a Prashant Deshlahra,^{b*} and Ya-Huei (Cathy) Chin^{a*}

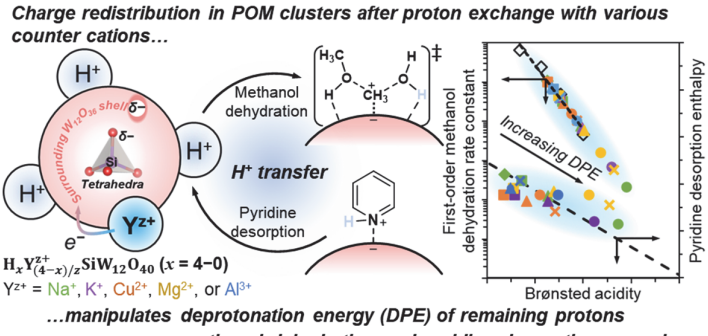
^aDepartment of Chemical Engineering and Applied Chemistry, University of Toronto, Toronto, Ontario M5S 3E5, Canada ^bDepartment of Chemical and Biological Engineering, Tufts University, Medford, Massachusetts 02155, United States *E-mails: Prashant.Deshlahra@tufts.edu; cathy.chin@utoronto.ca

ABSTRACT

Rigorous kinetic assessments, pyridine chemical titration and desorption, together with density functional theory (DFT) calculations establish the trends in the modulation of chemical identity, valence, site density and strength of Brønsted acid sites by counter cations (Na+, K+, Cu2+, Mg2+, and Al3+) on Keggin-type polyoxometalate tungstosilicic acid clusters (H₄SiW₁₂O₄₀, POM). Monovalent cations (Na⁺ and K⁺) exchange protons and decrease the acid strength of the residual protons, as indicated by the deprotonation energy (DPE) that increases from 1100 to 1175 kJ mol⁻¹ with increasing extent of proton exchange (decreasing the nominal H⁺-to-POM ratio). In contrast, di- and tri-valent cations preferentially exchange protons in the form of hydroxides $(Y^{z^+}(OH)_m, Y^{z^+} = Cu^{2^+}, Mg^{2^+}, \text{ or } Al^{3^+}, 0 < m < z)$, resulting in an average DPE value on both POM clusters and associated hydroxides ranging between 1100 and 1150 kJ mol⁻¹. A portion of these cations disperse on the silica support, generating Lewis acid sites. The exchanged cations modulate the charge within the $W_{12}O_{36}$ oxide shell, rather than the central SiO_4^{4-} tetrahedron, which mainly modifies the ionic component of DPE values. Monovalent cations with smaller electronegativity than di- and tri-valent cations donate more electrons, which increases the electrostatic interaction of residual protons with conjugate POM⁻ anions and leads to higher DPE (weaker acids). This study expands the library of Brønsted acidic catalysts with flexibility in tuning their acid strengths and densities, thus providing a series of samples for constructing structure-reactivity relationships and probing site electrostatic correlations on structurally constrained domains.

KEYWORDS: *POM cluster, Brønsted acid strength, cation exchange, deprotonation energy, methanol dehydration, electrostatic correlation, DFT calculations*

TABLE OF CONTENTS GRAPHIC



...methanol dehydration and pyridine desorption as probes

1. INTRODUCTION

Keggin-type polyoxometalate clusters (POM, H_{8-n}Xⁿ⁺M₁₂O₄₀) are well-described atomistic structures, constructed from an oxoanionic tetrahedral core with a central X^{n+} heteroatom ($XO_A^{(8-n)-}$), surrounded by a metal oxide shell (M₁₂O₃₆) with 8-n number of charge-balancing acidic protons (H⁺). ¹⁻³ Their well-defined atomic connectivity has rendered them ideal model catalysts for establishing the structures, thermochemical properties, and reactivity relationships in Brønsted acid catalyzed reactions.³⁻⁵ The number of protons on a POM cluster, 8-n, is given by the chemical identity, and specifically the valence, of the heteroatom X; their acid strength is quantitatively described by deprotonation energy (DPE), defined by the energy required to remove a proton from a neutral POM cluster to form an isolated proton and a structurally relaxed isolated conjugate POM anion (POM⁻) (H-POM \rightarrow H⁺ + POM⁻, $\Delta E = DPE$). As previously established, the DPE values serve as a rigorous kinetic descriptor for a wide range of Brønsted acid catalyzed reactions, e.g., alkanol dehydration,⁷⁻¹⁰ alkene oligomerization,^{11,12} and alkane isomerization reactions^{13,14} on H_{8-n}XW₁₂O₄₀ clusters $(X = S^{6+}, P^{5+}, Si^{4+}, Al^{3+}, or Co^{2+})$, 7-14 particularly for those proceeding via a late transition state, where the activation barriers for these reactions can be decomposed into various energetic components, including DPE, within a Born-Haber thermochemical framework between the precursors and the late, cationic type transition states.⁷

The Brønsted acid strength of POM clusters varies with the valence of central heteroatom X, the identity of the oxide shell, and the proton exchange with counter cations. 15-17 As an example, decreasing the valence electrons in heteroatom X from S⁶⁺, P⁵⁺, Si⁴⁺, Al³⁺, to Co²⁺ leads to a commensurate increase in DPE from 1068 to 1142 kJ mol⁻¹ on $H_{8-n}X^{n+}W_{12}O_{40}$ clusters. ^{18,19} Changing the oxide shell metal atom M from W⁶⁺ to Mo⁶⁺ causes an increase in DPE from 1105 to 1125 kJ mol⁻¹ on H₄SiM₁₂O₄₀ clusters. ^{18,19} Lastly, exchanging a portion of the charge-balancing protons with counter cations, such as Cs⁺ cations, ^{20–23} moderates the acid strength of remaining protons. These results suggest that changing the identity of counter cations to species such as Na⁺, K⁺, Cu²⁺, Mg²⁺, and Al³⁺ can further tune the acid strength, 5,24-28 which may

potentially broaden the range of accessible DPE values.

Previous NH₃-temperature programmed desorption (NH₃-TPD) and pyridine calorimetry and adsorption studies on $H_xCs_{3-x}PW_{12}O_{40}$ clusters (x = 2-0)^{20,29} and methanol dehydration kinetic interrogations on $H_xY_{(3-x)/2}PMo_{12}O_{40}$ clusters (x = 3-0, $Y^{z+} = Na^+$, Cu^{2+} , Mg^{2+} , and Al^{3+})^{30,31} have shown that such exchanges lead to a decrease in Brønsted acid strength of the remaining protons (increasing DPE values). Such effects are unlike those of microporous materials, e.g., zeolites, because ion-exchange could alter^{32,33} or not³⁴ the acid strength of remaining protons in microporous materials, depending on the spatial distribution of Brønsted sites.³⁵ In contrast, counter cations, when exchange with a portion of protons on POM clusters, would markedly modulate the acid strength of the remaining protons, simply because these protons are confined within the same cluster and that, after cation exchange, their charge would redistribute.^{36,37} Despite the mounting evidence, there is in general a lack of systematic study on how the chemical identity and the number of counter cations would mediate the Brønsted acid strength, what are the exact reasons behind the modulation, and extent of acid strength modulation have not yet been rigorously established.

Herein, we embark on a journey to probe and quantitatively establish how exchanging a portion of protons on solid Keggin-type tungstosilicic acid clusters (H4SiW₁₂O₄₀) with different counter cations Y^{z+} $(Y^{z+} = Na^+, K^+, Cu^{2+}, Mg^{2+}, or Al^{3+})$ and at different extents of proton exchange on $H_xY_{(4-x)/z}SiW_{12}O_{40}$ clusters (x = 4-0, denoted as $H_x Y_{(4-x)/z} Si$) would alter the Brønsted acid strength of remaining protons. Firstorder methanol dehydration rate constants, extracted from rigorous rate assessments, and pyridine desorption enthalpies from pyridine temperature programmed desorption, both demonstrate an increase in overall DPE values and thus a decrease in Brønsted acid strength, as the extent of proton exchange increases. Monovalent cations exhibit a more significant DPE modulation in the range of 1100-1175 kJ mol⁻¹ compared to that of di- and tri-valent cations in the range of 1100-1150 kJ mol⁻¹, concerning cation identities and the extent of proton exchange. We elucidate, through density functional theory (DFT) calculations, that the primary electronic modulation of counter cations occurs through their electron donation into the W₁₂O₃₆ oxide shell rather than the SiO₄⁴⁻ tetrahedral core. This modulation affects the ionic component of DPE, thus influencing the overall DPE value, along with its covalent counterpart. This series of cation exchanged POM clusters extends the repertoire of Brønsted acidic catalysts, adding another dimension in structural-compositional flexibility. This work illustrates the electrostatic correlations of Brønsted sites on structurally constrained POM clusters. The conceptual framework and methodology developed herein hold promise for rationalizing site correlations on broader catalysts as well.

2. EXPERIMENTAL SECTION

2.1. Preparation of Cation Exchanged $H_xY_{(4-x)/z}SiW_{12}O_{40}$ Clusters (x = 4-0, $Y^{z+} = Na^+$, K^+ , Cu^{2+} , Mg^{2+} , or Al^{3+}) Dispersed on High Surface Area Silica

Inert silica supported $H_xY_{(4-x)/z}SiW_{12}O_{40}$ clusters ($x = 4-0, Y^{z+} = Na^+, K^+, Cu^{2+}, Mg^{2+}, or Al^{3+}, z$ is the valence of Y^{z+} , surface density 0.14 POM nm⁻²), denoted hereinafter as $H_xY_{(4-x)/z}Si$, were prepared by incipient wetness impregnation method following previously reported procedures. 31,36,38 Before catalyst dispersion, the silica support (GRACE chromatographic grade, Code 1000188421, surface area 330 m² g⁻¹, particle size <75 μ m, pore volume 1.4 cm³ g⁻¹) was heated in air (Linde, grade 0.1, 0.1 cm³ (g_{cat} s)⁻¹) at 0.083 K s⁻¹ to 873 K and then maintained at 873 K for 4 h. During incipient wetness impregnation, an aqueous $H_x Y_{(4-x)/z} SiW_{12}O_{40}$ solution (x = 4-0, $Y^{z^+} = Na^+$, K^+ , Cu^{2+} , Mg^{2+} , or Al^{3+} , 1.4 cm³ $g_{SiO_2}^{-1}$), prepared by dissolving H₄SiW₁₂O₄₀ (Sigma-Aldrich, 99.9%) in double deionized water (>18.2 MΩ cm, 298 K) with the stoichiometric amount of sodium hydroxide (Fisher chemical, 97.0%), potassium hydroxide (Sigma-Aldrich, 99.99%), copper (II) carbonate basic (Sigma-Aldrich, 50.0–57.0% Cu basis), magnesium carbonate hydroxide hydrate (Sigma-Aldrich, 99%), or aluminum nitrate nonahydrate (Sigma-Aldrich, 99.997%), respectively, was added to the silica support dropwise under constant grinding rate in a ceramic mortar. The impregnated samples were then aged in ambient conditions for 24 h before treated in flowing helium (Linde, grade 5.0, 0.6 cm³ (g_{cat} s)⁻¹) at 0.017 K s⁻¹ to 323 K and held isothermally at 323 K for 24 h. After that, the dried samples were pressed into pellet using a die (Carver, 31 mm i.d.) and hydraulic press (Specac) at 130 MPa for 10 min. The pellet was crushed and then sieved to retain aggregates with particle diameters between 125 and 180 µm. H₄SiW₁₂O₄₀ clusters (H₄Si) with surface densities of 0.05 H₄Si nm⁻², 0.2 H₄Si nm⁻², and 0.4 H₄Si nm⁻² as well as reference samples of Na/SiO₂, K/SiO₂, Cu/SiO₂, Mg/SiO₂, and Al/SiO₂, containing sole proton exchange reagents (without POM clusters) such as hydroxides, carbonates, and nitrates with surface densities of 0.27 Na nm⁻², 0.27 K nm⁻², 0.27 Cu nm⁻², 0.27 Mg nm⁻², and 0.134 Al nm⁻², respectively, were prepared following identical procedures to those used for dispersing $H_x Y_{(4-x)/z} Si$ clusters on silica.

2.2. Pyridine Chemical Titration and Temperature Programmed Desorption (TPD)

The densities of total acid sites, including Brønsted (H⁺) and Lewis sites (LAS), of catalyst samples were determined by isothermal pyridine titration at 473 K, a temperature that was previously shown to minimize weakly adsorbed pyridine on both POM clusters and silica support,³⁶ followed by temperature programmed desorption (TPD) in flowing helium. The experiments were carried out in a U-shaped tubular quartz reactor (9.5 mm i.d.) ensuring plug flow hydrodynamics, placed in the middle of a furnace (Bluewater,

Microfurnace MFFC69120425) connected to a temperature controller (Omega, CN3251) via a thermocouple (K-type). During experiments, the catalyst samples (~100 mg), loaded in the quartz reactor, were treated in situ in flowing helium (Linde, grade 5.0, 0.83 cm³ s⁻¹) at 0.033 K s⁻¹ to 473 K and then kept isothermally at 473 K for 2 h, before pyridine titration at the same temperature. Liquid pyridine was then introduced, through a gastight syringe (SGE, Model 006230, 0.25 cm³) that was mounted on a syringe pump (KD Scientific, LEGATO 100), into a heated evaporation zone that was maintained at 383 K at a liquid volumetric flowrate commensurate with a pyridine partial pressure of ~0.1 kPa (2.1 µmol_{pvr} min⁻¹, subscript pyr denotes pyridine). Pyridine was quantified with an online gas chromatograph (GC, SRI, 8610C), equipped with an MXT-1 column (60 m, 0.53 mm i.d., 5.00 µm film) and a flame ionization detector (FID). In experiments, pyridine was first introduced to the bypass stream for ~2 h to ensure a stable pyridine partial pressure, confirmed with GC analysis, before it was introduced to the reactor. Pyridine titration was completed, when the pyridine pressure in the effluent equaled that of the feed pressure, at that point pyridine was removed from the feed stream. The catalyst bed was subsequently purged with pure helium (0.83 cm³ s⁻¹) for 1 h to remove physically adsorbed pyridine before the temperature programmed desorption (TPD) experiment. TPD was carried out at a constant temperature ramping rate of 0.167 K s⁻¹ to and maintained isothermally at 1000 K for 0.5 h in flowing helium (0.17 cm³ s⁻¹), and the pyridine desorption rate was recorded and quantified by the GC system. The total acid site density is determined by integrating the pyridine desorption rate during TPD, $F_{nvr,t}$ (10⁻³ µmol_{pyr} (µmol_{POM} s)⁻¹, per POM cluster), over the course of the TPD experiment, starting from time, t(s), equaled zero at the beginning of the experiment:

$$[T](POM^{-1}) = \int_0^t F_{pyr,t} \left(\frac{\mu mol_{pyr}}{\mu mol_{POM} s} \right) dt(s)$$
 (1a)

$$[T] = [H^+] + [LAS] \tag{1b}$$

The deconvolution of pyridine-TPD profiles was performed on PeakFit v4.12 software, following "AutoFit Peaks III Deconvolution" methodology after baseline correction using previously reported procedures.³⁹ These profiles were fitted with three sub-peaks for most of samples, and two peaks for the remaining samples. For all deconvoluted sub-peaks, the centers and full widths at half height (FWHH) of the peaks were allowed to vary, and the height of each peak was the dominant adjustable parameter. The multipeak fitting iteration was carried out with a coefficient of determination (R²) above 0.997.

2.3. Pyridine Infrared Absorption Spectra (IR)

The fractions of Brønsted and Lewis acid sites on the $H_xY_{(4-x)/z}Si$ cluster series (x = 4-0, $Y^{z^+} = Na^+$, K^+ , Cu^{2^+} , Mg^{2^+} , or Al^{3^+}) and the reference samples were determined by pyridine infrared absorption spectroscopy

(pyridine-IR) at 473 K following previously reported procedures.^{40,41} It was performed with a Bruker Vertex 70 spectrometer with an XSA attachment, SiC MIR globar source, HeNe interferometer, CaF₂ beamspliter and windows, and liquid nitrogen-cooled HgCdTe detector, using a custom-made transmission IR cell with temperature regulation (Staco Energy, Variable Autotransformer, Type 3PN1010), monitoring (Omega, DP1096), equipped with dynamic vacuum capability using a rotary vane pump (model 101150/11-11, Leroy Somer), and gas/liquid phase chemical introduction (described in detail in Section 2.2), where all gas lines were heated above 393 K to prevent condensation. All spectra were collected at 2 cm⁻¹ resolution, 3 mm aperture diameter, and 64 scans.

For each experiment, the catalyst sample was compressed into a self-supporting wafer (~1.3 cm in diameter and ~30 mg cm⁻² in surface density) with a thickness of less than 0.5 mm using a die set (Across International, 30 mm i.d.) and hydraulic press (Specac) at 63 MPa for 5 min. Prior to loading the sample, the cell was purged with flowing helium (0.83 cm³ s⁻¹) at 473 K for 0.5 h, followed by heating at the same temperature for another 0.5 h under vacuum (~0.05 mbar), before the collection of background spectrum. Then, the sample wafer was loaded onto a sample holder inside the cell, pretreated in helium (0.83 cm³ s⁻¹) at 0.033 K s⁻¹ to and kept isothermally at 473 K for 1 h to prevent the adsorption of water and hydrocarbons from the ambient atmosphere. Before pyridine introduction, the infrared absorption spectrum of the catalyst sample was obtained. Pyridine was then introduced (~0.1 kPa, with methods described in Section 2.2) until the sample was saturated with pyridine, where the intensity of pyridine absorption bands no longer varied. The sample chamber was then evacuated under dynamic vacuum to remove the gas phase and weakly adsorbed pyridine before spectroscopic measurements. All spectra were normalized with the vibrational bands corresponding to the lattice overtone of silica at 1990 cm⁻¹ and 1875 cm⁻¹ to allow quantitative comparisons of the peak intensities among the samples, following methods described elsewhere.⁴²

2.4. Steady-State Rate Measurements of Methanol Dehydration to Dimethyl Ether

Methanol dehydration to dimethyl ether (DME, CH₃OCH₃) was carried out in the temperature range of 393–493 K in a reactor system similar to that described in Section 2.2. During experiments, methanol was introduced, vaporized, and mixed with flowing helium (Linde, grade 5.0). The volumetric flowrate of helium carrier gas was controlled by mass flow controllers (Brooks Instrument, SLA5800 Series). The reactants and products were separated and quantified with an online gas chromatograph (Agilent 7890B) equipped with a capillary column (HP-PLOT/Q, 40 Micron, 30 m×0.53 mm) and an FID, which was connected with a methanizer (arc, JetanizerTM). In each experiment, 10-150 mg $H_xY_{(4-x)/z}Si$ clusters (x = 4-0, $Y^{z+} = Na^+$, K^+ , Cu^{2+} , Mg^{2+} , or Al^{3+} , 125-180 μm) were externally mixed with up to 140 mg of inert

silica (125–180 μ m), keeping the catalyst bed height constant. The catalyst was then heated in situ at 0.033 K s⁻¹ to 473 K and then kept isothermally at 473 K for 2 h in flowing helium (0.83 cm³ s⁻¹) before cooling to reaction temperatures for rate measurements.

2.5. Density Functional Theory (DFT) Calculations

Energies of POM clusters, their conjugate anions and isolated protons were calculated using plane-wave DFT methods within Vienna ab initio simulation package (VASP 5.4.4). 43,44 Gradient corrected Perdew-Burke-Ernzerhof (PBE) exchange correlation functional⁴⁵ with D3 dispersion correction and Becke-Johnson damping (D3BJ) method of Grimme et al. 46 was used to calculate electronic energies. Planewave basis sets up to a kinetic energy cutoff of 400 eV were used to determine electronic wavefunctions of valence electrons. Interactions of valence electrons with atomic cores treated using the projector augmented wave (PAW) method.⁴⁷ POM clusters, anions and proton were treated as isolated species in a 20 Å cubic supercell and a 1×1×1 Monkhorst-Pack k-point mesh was used to sample the first Brillouin zone.⁴⁸ The convergence criteria for electronic energy calculation and geometry optimization were $< 1 \times 10^{-5}$ eV energy change and < $0.05~eV~{\rm \AA^{-1}}$ maximum atomic force, respectively. Dipole and quadrupole corrections implemented within VASP⁴⁹ are used to correct for electrostatic interactions between periodic neighbors. Previous calculations have shown that such corrections give accurate energies of neutral and charged systems leading nearly identical to DPE values using periodic and molecular codes for cluster systems that do not contain atoms near the supercell boundary. 18 DPE values are calculated as energy required to form an isolated conjugate anion and an isolated proton from a neutral POM cluster ($DPE = E_{POM}^- + E_{H^+} - E_{POM}$). Classical Coulombic electrostatic interaction energy between the charge density of the relaxed isolated anion and the proton as a point charge placed at different distances from the anion is calculated to identify the distance at which this electrostatic interaction is the strongest without modifying anion charge density.⁶ The negative of this electrostatic interaction energy at the point of strongest interaction is taken as the ionic component of DPE $(E_{ion}^{H^+})$ as described previously.⁶ The difference between DPE and its ionic component is the energy associated with reorganizing the charge densities to form the neutral POM, which is considered the covalent component of DPE ($E_{cov}^{H^+} = DPE - E_{ion}^{H^+}$).

3. RESULTS AND DISCUSSION

3.1. Brønsted and Lewis Site Distributions on $H_xY_{(4-x)/z}Si$ Cluster Series (x = 4-0, $Y^{z+} = Na^+$, K^+ , Cu^{2+} , Mg^{2+} , or Al^{3+})

The structure of POM clusters, after dispersing them on silica support, has been well established in previous

studies on various unexchanged $H_3PW_{12}O_{40}^{50,51}$ and $H_4SiW_{12}O_{40}$ clusters,⁵⁰ as well as cation exchanged $H_xY_{(3-x)/2}PMo_{12}O_{40}$ clusters (x = 3-0, $Y^{z+} = Na^+$, Cu^{2+} , Mg^{2+} , or $Al^{3+})^{30,31,52}$ with wide ranging surface densities (0.04–1.35 POM nm⁻²). Transmission electron microscopy (TEM),⁵² which detects the cluster diameter, and X-ray diffraction (XRD),^{30,31,50,51} which identifies the characteristic diffraction patterns of different POM morphologies, e.g., 2D POM aggregates vs. 3D POM crystallites, reveal that the distributions of POM clusters on silica vary with POM surface density and counter cations, where higher surface densities and cation exchange cause cluster aggregation. Extending these findings to our studies, the unexchanged H₄Si clusters with surface densities of 0.05–0.14 POM nm⁻² are expected to predominantly exist as isolated POM clusters. In contrast, the H₄Si clusters with higher surface densities (0.2–0.4 POM nm⁻²) and the cation exchanged $H_xY_{(4-x)/2}Si$ clusters (x = 3-0, $Y^{z+} = Na^+$, K^+ , Cu^{2+} , Mg^{2+} , or Al^{3+} ; 0.14 POM nm⁻²) partially form 2D POM aggregates due to the bridging of different Keggin units by counter cations.

For the matrix library of $H_x Y_{(4-x)/z} Si$ clusters (x = 4-0, z = valence of cation Y^{z+}) with different cations, Y^{z+} (Na⁺, K⁺, Cu²⁺, Mg²⁺, or Al³⁺), and, for each cation, with different nominal H⁺-to-POM ratios (x = 4-0), at a constant surface density of 0.14 POM nm⁻², their pyridine desorption profiles during temperature programmed desorption (pyridine-TPD) and infrared absorption spectra with pyridine as a probe molecule (pyridine-IR) are shown in Figure 1a–c for Na⁺ exchanged clusters (H_x Na_{4-x}Si, x = 4-0) and in Figures S1–4 of the Supporting Information for K⁺, Cu²⁺, Mg²⁺, and Al³⁺ exchanged clusters. Taking the example of $H_xNa_{4-x}Si$ clusters (x = 4-0), pyridine-TPD (Figure 1a) gives the total acid site density ([T], per POM cluster), and the peak deconvolution of the profiles (Figure 1b) provides trends in acid strength. First, the cumulative pyridine desorption per POM cluster equals the total acid site density, which equals the sum of Brønsted and Lewis sites, at a stoichiometry of one adsorbed pyridine per site. 36,53 Second, their pyridine infrared absorption spectra (Figure 1c) give the fractions of Brønsted and Lewis sites, derived from the absorption peak intensity ratio of 1540 to 1450 cm⁻¹, which correspond to pyridinium ion at Brønsted sites and molecularly adsorbed pyridine at Lewis sites, respectively, assuming a Brønsted-to-Lewis site extinction coefficient $(\varepsilon_{\text{Brønsted}}(\varepsilon_{\text{Lewis}})^{-1})$ of 0.75.^{36,54} These results, taken together, give the Brønsted and Lewis site densities, $[H_{pyr\,TPD-IR}^+]$ and $[LAS_{pyr\,TPD-IR}]$ (per POM cluster), in Figure 2a,b, respectively, for the complete library of $H_xY_{(4-x)/z}S_i$ catalysts (x = 4-0), arranging with increasing valence of cations (Na⁺, K⁺, Cu²⁺, Mg²⁺, then Al³⁺), as also tabulated together with their fractions in Table S1 of the Supporting Information.

A clear trend begins to emerge for clusters with monovalent cations ($Y^{z^+} = Na^+$ or K^+ , Figure 1a and Figure S1a of the Supporting Information). Pyridine desorption began at ~550 K, irrespective of the identity

of counter cations (Na⁺ or K⁺) and their nominal H⁺-to-POM ratios. For clusters exchanged with a given monovalent cation Y^{z+} (Na⁺ or K⁺), pyridine desorption completed at a lower temperature and the maximum pyridine desorption rate decreased with decreasing the nominal H⁺-to-POM ratio. For clusters with di- or trivalent cations ($Y^{z+} = Cu^{2+}$, Mg^{2+} , or Al^{3+} , Figures S2a–4a of the Supporting Information), their pyridine-TPD profiles exhibited greater complexity compared to those with monovalent cations ($Y^{z+} = Na^{+}$ or K^{+}). In general, pyridine desorption rates in the low temperature range (600–700 K, $H_xY_{(4-x)/z}Si$, $Y^{z+} = Cu^{2+}$ or Mg^{2+} , Figures S2a and S3a of the Supporting Information) and the maximum pyridine desorption rates ($H_xAl_{(4-x)/2}Si$, Figure S4a of the Supporting Information) increased with decreasing the nominal H⁺-to-POM ratio. These changes likely reflect the creation of additional Brønsted and Lewis sites through cation exchange. ^{31,55}

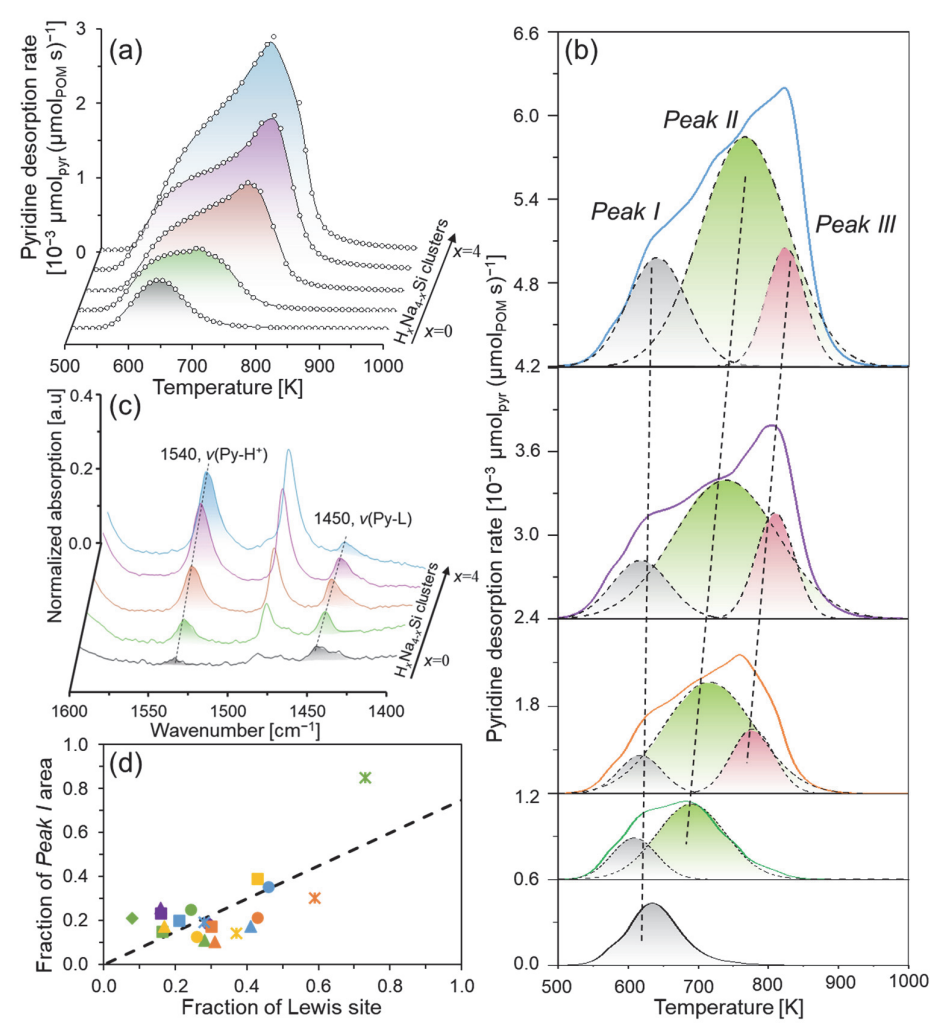


Figure 1. (a) Profiles of pyridine temperature programmed desorption (TPD), (b) deconvolution of pyridine-TPD profiles with *Peaks I–III* (500–700, 550–850, and 710–870 K), and (c) pyridine infrared absorption spectra with the characteristic peaks of pyridinium ion at Brønsted sites (1540 cm⁻¹) and of molecular pyridine at Lewis sites (1450 cm⁻¹), on $H_xNa_{4-x}Si$ clusters (x = 4-0; black, x = 0; green, x = 1; yellow, x = 2; purple, x = 3; blue, x = 4). (d) Correlations between the fraction of *Peak I* area derived from pyridine-TPD profiles, and the fraction of Lewis site density, derived from pyridine-IR studies (Table S1 of the Supporting Information) for the $H_xY_{(4-x)/z}Si$ cluster series (x = 4-0, $Y^{z+} = Na^+$ (green), K^+ (purple), Cu^{2+} (orange), Mg^{2+}

(yellow), or A1³⁺ (blue). Diamond, x = 4; square, x = 3; triangle, x = 2; circle, x = 1; cross, x = 0). Dashed lines represent trends and are intended to guide the eyes.

These desorption profiles are further deconvoluted into three sub-desorption peaks within the temperature ranges of 500-700, 550-850, and 710-870 K, as Peaks I, II, and III, respectively (Figure 1b and Figures S1b-4b of the Supporting Information). Irrespective of the nominal H⁺-to-POM ratio, the temperature corresponding to the maximum pyridine desorption of *Peak I* remained at the same position, except for the $H_xAl_{1.33-0.33x}Si$ (x = 4-0) cluster series, which exhibited disparate pyridine-TPD behavior compared to others, probably because of the strong Lewis acid strength of Al³⁺ cations (Figure S5a of the Supporting Information). Unlike Peak I, the maximum desorption temperatures for Peaks II and III shifted to lower temperatures with decreasing the nominal H⁺-to-POM ratio, e.g., ~60 K for clusters with monovalent cations and ~30 K for those with di- or tri-valent cations. The fraction of pyridine desorbed in the lowest temperature range (500–700 K), derived from the ratio of area of *Peak I* to that of all peaks, appears to correlate to the fraction of Lewis sites (Figure 1d), derived from pyridine-IR studies. This correlation suggests that pyridine desorbs from Lewis sites at the lower temperatures (Peak I) and from Brønsted sites at the higher temperatures (Peaks II and III), similar with previous pyridine-TPD peak assignments for sites in ion-exchanged zeolites, e.g., M^{n+} -ZSM-5 (M^{n+} = $A1^{3+}$, Ca^{2+} , and Ba^{2+}). ³⁴ The decrease in the maximum pyridine desorption temperatures of *Peaks II* and *III* strongly suggests a decrease in Brønsted acid strength for the remaining protons, when a portion of protons are replaced by counter cations.

We note that, on clusters without counter cation exchange (H₄Si), Lewis sites essentially do not exist, determined to be ~0.17 *LAS POM*⁻¹, a small value that is most likely originating from structural defects of POM clusters, where the breakage of W–O linkages exposes the coordinatively unsaturated cationic metal centers, Wⁿ⁺, as an electron acceptor with Lewis acid characters. Exchanging protons with monovalent cations, Na⁺ or K⁺, would monotonically decrease the Brønsted site density—each addition of Na⁺ or K⁺ titrated ~0.47±0.01 H⁺, whereas the Lewis site density kept relatively constant and negligible at ~0.2±0.05 *LAS POM*⁻¹ (H_xY_{(4-x)/2}Si, x = 4–0, Y^{z+} = Na⁺ or K⁺, Figure 2b). In contrast, exchanging protons with di- or tri-valent cations, Cu²⁺, Mg²⁺, or Al³⁺, led Brønsted site density to decrease in a much lower rate—in fact, each addition of Y^{z+}z⁻¹ cation (i.e., Cu²⁺, Mg²⁺, and Al³⁺ cations divided by their valence) titrated only ~0.20±0.04 H⁺; whereas their Lewis site density increased to ~0.64±0.25 *LAS POM*⁻¹ (H_xY_{(4-x)/2}Si, x = 3–0, Y^{z+} = Cu²⁺, Mg²⁺, or Al³⁺, Figure 2b) and remained insensitive to the extent of cation exchange. This relatively constant Lewis site density is likely because the di- or tri-valent cations promote the aggregation

of POM clusters, where a cation interacts with multiple Keggin units, forming bridged bonds $(Y^{z^+}-(POM)_q, q > 1)$ to satisfy their charge balance. We note that stoichiometric exchange, which requires for maintaining the overall charge balance of the cluster, e.g., 1 Na⁺ exchanging with 1 H⁺ and 1 Cu²⁺ exchanging with 2 H⁺, was not attained, indicating that a portion of cations is dispersed on the surface of silica.³¹

In an attempt to correlate Brønsted and Lewis site distributions on $H_xY_{(4-x)/z}Si$ clusters with the counter cation identity, we consider two scenarios: $H_xY_{(4-x)/z}Si$ clusters with monovalent cations $(Y^{z+} = Na^+ \text{ or } K^+)$ and those with di- or tri-valent cations $(Y^{z+} = Cu^{2+}, Mg^{2+}, \text{ or } Al^{3+})$, together with the dispersion of these cations on silica, shown in Scheme 1. Monovalent cations substitute protons on H₄Si clusters, leading to a monotonic decrease in Brønsted site density, as the extent of proton exchange increases and the nominal H⁺-to-POM ratio decreases. A small proportion of these cations interacts with silanol groups on silica, forming non-Lewis acidic centers due to their charge saturation. However, di- or tri-valent cations substitute protons on POM clusters, appearing either as cationic Y^{z+} or hydroxylated $Y^{z+}(OH)_m$ species (0 < m < z) resulting from water interaction with Y^{z+} cations. 5.15,56-58 A significant fraction of these cations disperse on silica, forming either Lewis $(Y^{z+}$ centers) or weak Brønsted sites $(Y^{z+}(OH)_m \text{ groups})$, 27,28 confirmed from separate pyridine-TPD and pyridine-IR studies on reference samples that contain only the dispersed cations on silica (without H₄Si clusters), as described in detail in Section S2 of the Supporting Information. These factors contribute to a slower decrease in Brønsted site density and the formation of Lewis sites on $H_xY_{(4-x)/z}Si$ clusters with di- or tri-valent cations $(Y^{z+} = Cu^{2+}, Mg^{2+}, \text{ or } Al^{3+})$ compared to those with monovalent cations $(Y^{z+} = Na^+ \text{ or } K^+)$ with decreasing the nominal H⁺-to-POM ratio.

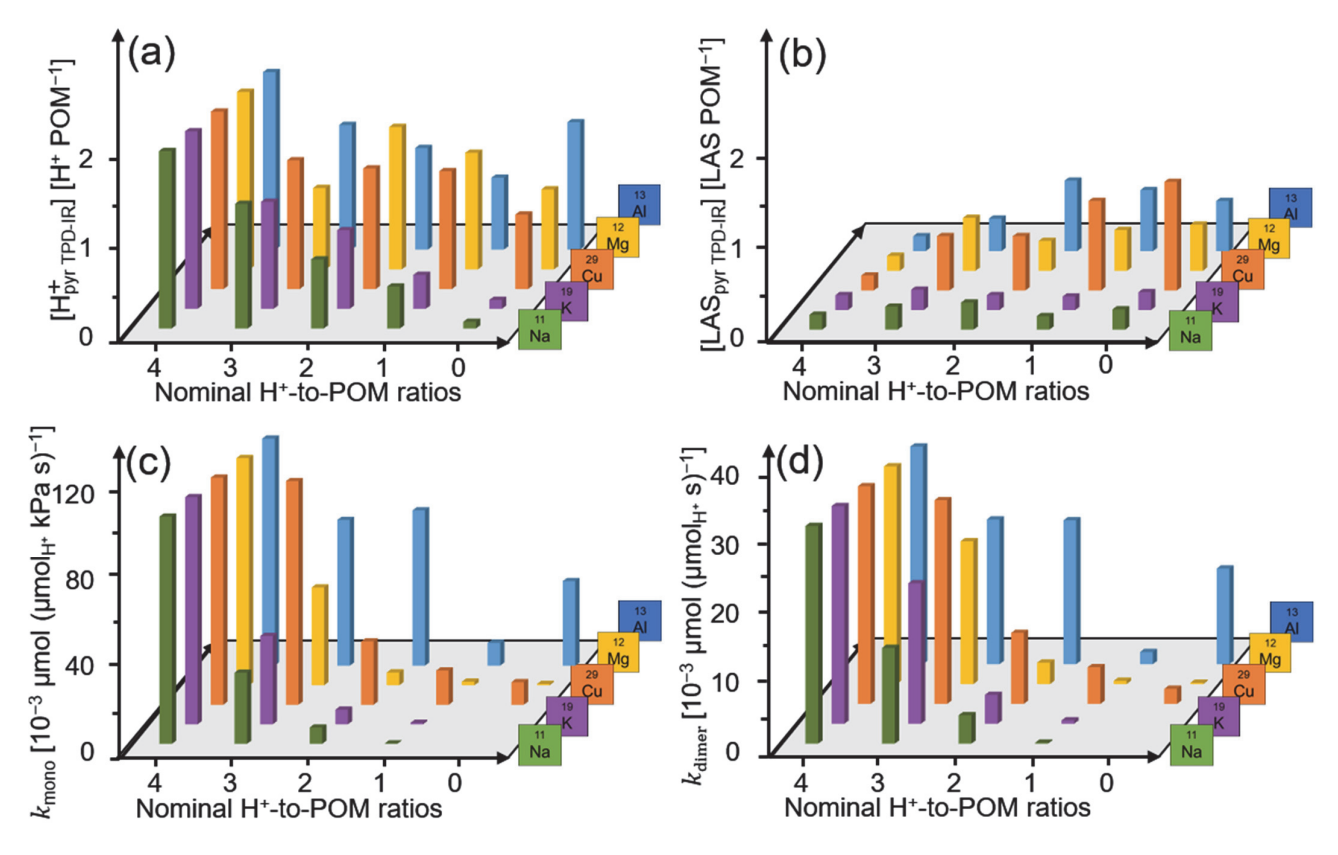
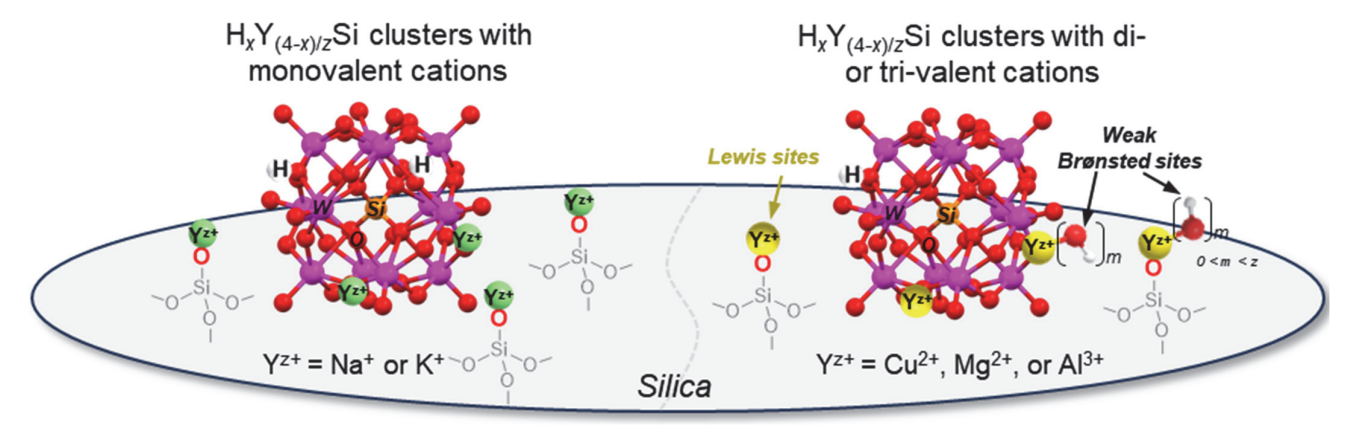


Figure 2. (a) Brønsted ($[H_{pyr\ TPD-IR}^+]$) and (b) Lewis site ($[LAS_{pyr\ TPD-IR}]$) densities (per POM cluster) derived from pyridine-TPD and pyridine-IR studies; (c) rate constants k_{mono} (= K_Dk_{C-O} , eq 4c, per H⁺) and (d) rate constants k_{dimer} (= k_{C-O} , eq 4d, per H⁺) of methanol dehydration to dimethyl ether at 433 K, as a function of the nominal H⁺-to-POM ratio on the $H_xY_{(4-x)/z}Si$ cluster series (x = 4-0, $Y^{z+} = Na^+$, K^+ , Cu^{2+} , Mg^{2+} , or Al^{3+}).

Scheme 1. Schematic Illustrations of $H_xY_{(4-x)/z}Si$ Clusters with Monovalent Cations (Left, $Y^{z^+} = Na^+$ or K^+) and Di- or Tri-Valent Cations (Right, $Y^{z^+} = Cu^{2^+}$, Mg^{2^+} , or Al^{3^+}), and the Dispersion of These Cations on Silica as Lewis and Weak Brønsted Sites



3.2. Assessments of Methanol Dehydration Turnover Rates at Brønsted and Lewis Sites on the $H_xY_{(4-x)/z}Si$ Cluster Series $(x = 4-0, Y^{z+} = Na^+, K^+, Cu^{2+}, Mg^{2+}, or Al^{3+})$

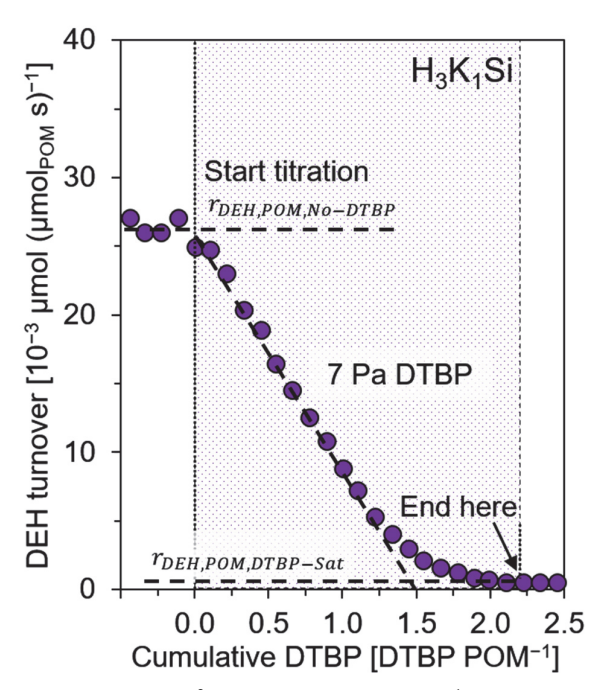


Figure 3. Methanol DEH turnover rates $(10^{-3} \mu \text{mol} (\mu \text{mol}_{POM} \text{ s})^{-1})$ as a function of cumulative 2,6-di-*tert*-butylpyridine (DTBP POM⁻¹) on H₃K₁Si clusters during in situ DTBP titration (3 kPa methanol, 7 Pa DTBP, $0.12 \text{ cm}^3 (\mu \text{mol}_{POM} \text{ s})^{-1}$, 433 K).

Table 1. Comparison of Brønsted Site Densities (per POM Cluster) Derived from In Situ DTBP Titration ($[H^+_{in-situ\ DTBP}]$) and Those from Pyridine-TPD and Pyridine-IR Studies ($[H^+_{pyr\ TPD-IR}]$), and Summary of the Ratios of Intrinsic Methanol DEH Turnover Rates at Brønsted Sites to Those at Lewis Sites ($r_{DEH,H^+}(r_{DEH,LAS})^{-1}$)

| POM^a | $[H_{in-situ\ DTBP}^+]^b$ | $\left[H_{pyrTPD-IR}^{+}\right]^{c}$ | $r_{DEH,H} + (r_{DEH,LAS})^{-1 d}$ |
|-----------------------------------|---------------------------|--------------------------------------|------------------------------------|
| H ₂ Na ₂ Si | 0.9 | 0.8 | 55 |
| H₃K₁Si | 1.5 | 1.2 | 13 |
| H_0Cu_2Si | 0.8 | 0.9 | 30 |
| H_0Mg_2Si | 0.5 | 0.9 | 4 |
| H₁Mg₁.₅Si | 1.1 | 1.3 | 10 |
| H ₁ AI ₁ Si | 0.8 | 8.0 | 11 |

^aSelected POM clusters with the highest Lewis site density (Table S1 of the Supporting Information) among their respective cation exchanged $H_xY_{(4-x)/2}Si$ cluster series ($Y^{z+} = Na^+$, K^+ , Cu^{2+} , Mg^{2+} , or Al^{3+}). ^bObtained from in situ DTBP titration displayed in Figure 3 and Figure S6 of the Supporting Information. ^cDerived from pyridine-TPD and pyridine-IR studies displayed in Table S1 of the Supporting Information. ^dRatios of methanol DEH turnover rates at Brønsted sites (H^+) to that at Lewis sites (LAS), calculated with eq 3 based on the rate depression during in situ DTBP titration.

CH₃OCH₃), at Brønsted and Lewis sites in the presence of 2,6-di-tert-butylpyridine (DTBP) titrants. Due to its steric hindrance, DTBP would selectively titrate Brønsted sites but not Lewis sites.⁵⁹ Figure 3 shows the time-dependent methanol DEH turnover rates (10⁻³ µmol (µmol_{POM} s)⁻¹), derived from the site-time-yield of DME formation, as a function of cumulative DTBP introduced (in DTBP POM⁻¹) during in situ DTBP incorporation (7 Pa) into the methanol feed on H₃K₁Si clusters at 433 K; Figure S6 of the Supporting Information shows similar profiles for H₂Na₂Si, H₀Cu₂Si, H₀Mg₂Si, H₁Mg_{1.5}Si, and H₁Al₁Si clusters. These clusters were selected, because they contain the highest Lewis site density (0.2-1.2 LAS POM⁻¹) among their respective cluster series. As shown in these figures, methanol DEH turnover rates decreased largely linearly throughout the titration, before levelling off to a lower value with DTBP incorporation. Linear extrapolation of the turnover suppression profile to x-intersect gives the Brønsted site density $([H_{in \, situ-DTBP}^+], \text{ per POM cluster})$. These results $([H_{in \, situ-DTBP}^+])$ for the selected $H_x Y_{(4-x)/z} Si$ clusters are consistent with the Brønsted site densities derived from pyridine-TPD and pyridine-IR studies $([H_{pyr\,TPD-IR}^+],$ in Section 3.1), and summarized in Table 1. When the turnover rates reached a lower and stable value, the titration was completed, where all Brønsted sites were occupied and unavailable for turnovers, leaving Lewis sites the only catalytically active sites. Removal of DTBP did not recover the DEH turnovers, indicating that Brønsted site occupation by DTBP is irreversible. The overall methanol DEH turnover rates before DTBP titration $(r_{DEH,POM,No-DTBP})$ and after DTBP saturation $(r_{DEH,POM,DTBP-Sat})$ are:

Next, we investigate the turnovers of methanol dehydration (DEH), which forms dimethyl ether (DME,

$$r_{DEH,POM,No-DTBP} = r_{DEH,H^{+}} \times \left[H_{pyr\,TPD-IR}^{+}\right] + r_{DEH,LAS} \times \left[LAS_{pyr\,TPD-IR}\right]$$
(2a)

$$r_{DEH,POM,DTBP-Sat} = r_{DEH,LAS} \times \left[LAS_{pyrTPD-IR} \right]$$
 (2b)

where r_{DEH,H^+} and $r_{DEH,LAS}$ are methanol DEH turnover rates (per H⁺ or LAS site) at Brønsted and Lewis sites, respectively, as denoted by their respective subscripts.

For monovalent cation exchanged clusters (e.g., H₂Na₂Si and H₃K₁Si, ~ 0.2 LAS POM⁻¹, in Figure S6a of the Supporting Information and Figure 3, respectively) that contain predominantly Brønsted sites, the near complete suppression of DEH turnovers, $r_{DEH,POM,DTBP-Sat}$, after DTBP saturation suggests that the term $r_{DEH,LAS} \times [LAS_{pyr\ TPD-IR}]$ is negligible, therefore the rate contributions of Lewis sites are insignificant. Within each series of di- and tri-valent cation exchanged clusters (e.g., H₀Cu₂Si, H₀Mg₂Si, H₁Mg_{1.5}Si, and H₁Al₁Si, 0.5–1.2 LAS POM⁻¹, Figure S6b–e of the Supporting Information), which contain both Brønsted and Lewis sites, methanol DEH turnover rates after DTBP saturation were significantly lower than their initial before **DTBP** incorporation. The depression, defined rates rate by 1 – $r_{DEH,POM,DTBP-Sat}(r_{DEH,POM,No-DTBP})^{-1}$, exceeds 0.93 for all clusters, except for the H₀Mg₂Si cluster (0.52 LAS POM⁻¹), which exhibits the smallest rate depression with a value exceeding 0.85 (Table S2 of the Supporting Information). Starting from eq 2a,b, the ratio of the intrinsic methanol DEH turnover rate at Brønsted sites to that at Lewis sites, r_{DEH,H^+} ($r_{DEH,LAS}$)⁻¹, is (see derivation in Section S3 of the Supporting Information):

$$\frac{r_{DEH,H^+}}{r_{DEH,LAS}} = \frac{1 - r_{DEH,POM,DTBP-Sat}(r_{DEH,POM,No-DTBP})^{-1}}{r_{DEH,POM,DTBP-Sat}(r_{DEH,POM,No-DTBP})^{-1}} \times \frac{[LAS_{pyrTPD-IR}]}{[H_{pyrTPD-IR}]}$$
(3)

Table 1 shows the results on the selected $H_xY_{(4-x)/z}Si$ clusters—methanol DEH turnover rates are about one order of magnitude higher at Brønsted sites than at Lewis sites (4–60× higher, 433 K). Separate experiments show negligible methanol DEH turnover rates at Lewis sites on the reference sample Al/SiO₂ (0.134 Al nm⁻²) compared to those at Brønsted sites on H₄Si clusters (Figure S7 of the Supporting Information). All these results together confirm that Brønsted sites but not Lewis sites catalyze most of the methanol DEH turnovers under our experimental conditions (433 K).

Previous kinetic assessments,⁸ isotopic labelling studies,⁵² and DFT calculations^{6,8} have established that methanol DEH reaction occurs via an associative mechanism at Brønsted sites. Scheme 2 (left panel) shows the reaction coordinate leading to the formation of the kinetically relevant transition state (TS). The reaction begins with equilibrated methanol adsorption at a proton through its O atom, forming a CH₃OH···H⁺····POM⁻ species (*CH*₃*OH* monomer, Step 1-Ads mono, K_M). Another methanol then adsorbs and undergoes protonation, forming a protonated *CH*₃*OH* dimer, (CH₃OH····CH₃····CH₃OH)····POM⁻, in equilibrium with methanol monomer (Step 2-Ads dimer, K_D). Next, the dimer undergoes an associative dehydration pathway, mediated by a carbocationic [(CH₃OH····CH₃+····H₂O)···POM⁻][‡] transition state (Step 3-Dehydration, k_{C-O}), forming a C-O bond and ejecting a water molecule before the desorption of dimethyl ether (CH₃OCH₃) to regenerate the Brønsted site. The alternative dissociative pathway (not displayed in Scheme 2), which involves the dehydration of the monomer and formation of a surface-bound methoxy species before the kinetically relevant nucleophilic attack by another methanol, has been previously ruled out based on DFT calculations on the series of H_{8-n}Xⁿ⁺W₁₂O₄₀ clusters (Xⁿ⁺ = P⁵⁺, Si⁴⁺, Al³⁺, or Co²⁺).⁸

Applying quasi-equilibrium assumptions (QE) on the two methanol adsorption steps (*Steps 1* and 2) and treating the C–O bond formation (*Step 3*) as the sole rate limiting step, but neglecting the adsorption of both DME and water, the products, at Brønsted sites due to their low partial pressures during reactions, this associative pathway gives the rate expression (r_{DEH,H^+} , per H⁺ site, detailed derivation in Section S4 of the Supporting Information) of methanol DEH turnovers, when methanol monomer and dimer co-exist and are

the most abundant surface intermediates (MASI), as previously established on POM clusters (H₄SiW₁₂O₄₀ and H₃PW₁₂O₄₀) and various zeolites (H-BEA, H-MFI, and H-USY, etc.):^{8,9,40,60}

$$r_{DEH,H^{+}} = \frac{k_{C-O}K_{M}K_{D}P_{CH_{3}OH}^{2}}{K_{M}P_{CH_{3}OH} + K_{M}K_{D}P_{CH_{3}OH}^{2}}$$
(4a)

$$=\frac{k_{mono} P_{CH_3OH}}{1 + \frac{k_{mono}}{k_{dimer}} P_{CH_3OH}} \tag{4b}$$

$$k_{mono} = K_D k_{C-O} (4c)$$

$$k_{dimer} = k_{C-O} \tag{4d}$$

Where K_M , K_D and k_{C-O} are methanol adsorption equilibrium constants for methanol monomer and dimer formations, and rate constant for the elementary C-O bond formation, respectively. Eq 4a reduces to eq 4b by defining (i) the first-order rate constant k_{mono} as the product of K_D and k_{C-O} (eq 4c) and (ii) the zero-order rate constant k_{dimer} as the sole k_{C-O} (eq 4d).

Figure S8 of the Supporting Information shows kinetic dependencies of methanol DEH turnover rates (per H⁺ site) on methanol pressure (0.05–0.8 kPa) at 433 K, after accounting for active site losses and catalyst deactivation, by extrapolating the rate data back to the initial time with a reference condition, as described elsewhere. For the entire $H_xY_{(4-x)/z}Si$ cluster series (x = 4-0, $Y^{z+} = Na^+$, K^+ , Cu^{z+} , Mg^{z+} , or Al^{3+}), the turnover rates exhibit similar dependencies on methanol pressure, where they initially increased linearly and then became insensitive to methanol, as methanol pressure increases. We note that, at such low methanol partial pressures (0.05–0.8 kPa) and relatively high reaction temperature (433 K) used for kinetic interrogation here, the formation of adsorbed trimeric methanol species, ((CH₃OH)₃····H⁺)····POM⁻, is negligible, especially at unconfined Brønsted sites prevalent on POM clusters, unlike those found in a confined void at high methanol pressures (>10 kPa, CHA, AEI, LEV, and LTA zeolites). Regression of the rate data displayed in Figure S8 of the Supporting Information against eq 4b gives the rate constants k_{mono} (eq 4c) and k_{dimer} (eq 4d) for the entire cluster series. The regressed kinetic parameters are reported in Figure 2c,d and their numerical values are summarized in Table S3 of the Supporting Information.

3.3. Interpretations of C-O Bond Formation Rate Constants in Methanol Dehydration and Derived DPE Values for $H_xY_{(4-x)/z}Si$ Cluster Series $(x = 4-0, Y^{z+} = Na^+, K^+, Cu^{2+}, Mg^{2+}, or Al^{3+})$

 k_{mono} , which equals $K_D k_{C-O}$, captures the Gibbs free energy change $(\Delta G_{mono}^{\dagger})$ required for evolving the $[(CH_3OH\cdots CH_3^+\cdots H_2O)\cdots POM^-]^{\dagger}$ transition state from a methanol monomer $(CH_3OH\cdots H^+\cdots POM^-)$. Expanding K_D with van't Hoff relation and k_{C-O} with transition state theory gives:

$$k_{mono} = \frac{k_B T}{h} exp \left(-\frac{\Delta G_{mono}^{\dagger}}{RT} \right)$$

$$= K_D k_{C-O}$$

$$= \frac{k_B T}{h} exp \left(\frac{\Delta S_D}{R} \right) exp \left(-\frac{\Delta H_D}{RT} \right) exp \left(\frac{\Delta S_{C-O}^{\dagger}}{R} \right) exp \left(-\frac{\Delta H_{C-O}^{\dagger}}{RT} \right)$$

$$= \frac{k_B T}{h} exp \left(\frac{\Delta S_{mono}^{\dagger}}{R} \right) exp \left(-\frac{\Delta H_{mono}^{\dagger}}{RT} \right)$$
(5a)

where
$$\Delta H_{mono}^{\ddagger} = \Delta H_D + \Delta H_{C-O}^{\ddagger}$$
 (5b)

and
$$\Delta S_{mono}^{\ddagger} = \Delta S_D + \Delta S_{C-O}^{\ddagger}$$
 (5c)

The activation enthalpy $\Delta H_{mono}^{\ddagger}$ reflects the sum of adsorption enthalpy ΔH_D and activation enthalpy $\Delta H_{C-O}^{\ddagger}$ for the evolvement of the transition state. Similar relation applied also to the activation entropy. The compensation effects of activation enthalpy and entropy^{63,64} allow us to connect between $\Delta S_{mono}^{\ddagger}$ and $\Delta H_{mono}^{\ddagger}$ with the following linear relation with a slope α_{mono} and an intercept β_{mono} :

$$\Delta S_{mono}^{\dagger} = \alpha_{mono} \Delta H_{mono}^{\dagger} + \beta_{mono}$$
 (5d)

Substitution of the entropic term in eq 5a with eq 5d gives:

$$k_{mono} = \frac{k_B T}{h} exp\left(\frac{\beta_{mono}}{R}\right) exp\left(-\frac{(1 - \alpha_{mono} T)\Delta H_{mono}^{\ddagger}}{RT}\right)$$
$$= A_{mono} exp\left(-\frac{(1 - \alpha_{mono} T)\Delta H_{mono}^{\ddagger}}{RT}\right)$$
(5e)

where
$$A_{mono} = \frac{k_B T}{h} exp\left(\frac{\beta_{mono}}{R}\right)$$
 (5f)

Similarly, k_{dimer} captures the Gibbs free energy change $(\Delta G_{dimer}^{\ddagger})$ required to evolve the same transition state from a methanol dimer. Following similar methods connecting $\Delta S_{mono}^{\ddagger}$ to $\Delta H_{mono}^{\ddagger}$ outlined in eq 5d above, k_{dimer} becomes:

$$k_{dimer} = \frac{k_B T}{h} exp \left(-\frac{\Delta G_{dimer}^{\dagger}}{RT} \right)$$

$$= k_{C-O}$$

$$= \left[\frac{k_B T}{h} exp\left(\frac{\Delta S_{C-O}^{\ddagger}}{R}\right)\right] exp\left(-\frac{\Delta H_{C-O}^{\ddagger}}{RT}\right)$$

$$= A_{dimer} exp\left(-\frac{(1-\alpha_{dimer}T)\Delta H_{dimer}^{\ddagger}}{RT}\right)$$
(6a)

where
$$A_{dimer} = \frac{k_B T}{h} exp\left(\frac{\beta_{dimer}}{R}\right)$$
 (6b)

and
$$\Delta H_{dimer}^{\ddagger} = \Delta H_{C-Q}^{\ddagger}$$
 (6c)

 k_B refers to Boltzmann constant, h the Planck constant, R the ideal gas constant, and T the temperature. Therefore, at a constant temperature, k_{mono} and k_{dimer} are single-valued functions of $\Delta H_{mono}^{\ddagger}$ and $\Delta H_{dimer}^{\ddagger}$ (eqs 5e and 6a), respectively, in methanol dehydration on the series of $H_xY_{(4-x)/z}Si$ clusters (x = 4-0, $Y^{z+} = Na^+$, K^+ , Cu^{2+} , Mg^{2+} , or Al^{3+}).

Born-Haber thermochemical cycle, 10,65 as depicted in Scheme 2 (left panel), decouples $\Delta H_{mono}^{\ddagger}$ and $\Delta H_{dimer}^{\ddagger}$ into accessible thermochemical properties of catalysts and reactants, as well as interactions between reactant fragments and catalytic surfaces. First, the POM cluster undergoes deprotonation (*Step BH.1*), forming a free proton (H⁺) and a conjugate POM anion (POM⁻), where the energy change equals its deprotonation energy (DPE). Next, the free proton combines with the two methanol molecules, followed by the rearrangement of one of methyl groups and charge transfer to form the analog of the transition state structure (CH₃OH····CH₃⁺····H₂O, *Step BH.TS_{unbound}*), unbound in the gas phase, with an energy change $E_{prot,ana}$. This cationic, unbound transition state analog then interacts with the conjugate POM⁻ anion, assembling the transition state structure (*Step BH.TS_{bound}*) by releasing energy, which equals the interaction energy $E_{int,ana}$. By exploiting the state function character of all relevant thermodynamic properties, $\Delta H_{mono}^{\ddagger}$ and $\Delta H_{dimer}^{\ddagger}$ become:

$$\Delta H_{mono}^{\ddagger} = DPE + E_{prot,ana} + E_{int,ana} - \Delta H_{M}$$
 (7a)

$$\Delta H_{dimer}^{\ddagger} = DPE + E_{prot,ana} + E_{int,ana} - \Delta H_M - \Delta H_D$$
 (7b)

In terms of the individual energy, the DPE of POM clusters depends strongly on the chemical identity of the central atom X, ranging from 1068 kJ mol⁻¹ for H₂SW₁₂O₄₀ to 1142 kJ mol⁻¹ for H₆CoW₁₂O₄₀ clusters;¹⁸ $E_{prot,ana}$ is an intrinsic property of gaseous methanol molecules and equals -815 kJ mol⁻¹;^{6,18,19} $E_{int,ana}$ reflects predominantly the electrostatic interactions between the gaseous transition state analog (CH₃OH····CH₃+····H₂O) and the conjugate POM⁻ anion.⁷ These terms, $E_{int,ana}$, ΔH_M , and ΔH_D , all depend on and could compensate the DPE value to varying extents, thus dampening the sensitivity of activation

enthalpies, $\Delta H_{mono}^{\ddagger}$ and $\Delta H_{dimer}^{\ddagger}$, to DPE values. $\Delta H_{mono}^{\ddagger}$ (or $\Delta H_{dimer}^{\ddagger}$) varies with DPE via a coefficient χ_{mono} (or χ_{dimer}), which ranges between zero and one, and a constant ψ_{mono} (or ψ_{dimer}):^{8,18}

$$\Delta H_{mono}^{\ddagger} = \chi_{mono} DPE + \psi_{mono}$$
 (8a)

$$\Delta H_{dimer}^{\ddagger} = \chi_{dimer} DPE + \psi_{dimer}$$
 (8b)

Previous kinetic studies and DFT calculations⁸ have established the strong dependencies of k_{mono} and k_{dimer} values (derived in 0.05–0.8 kPa methanol at 433 K) on DPE, i.e., from 1087 to 1140 kJ mol⁻¹, as the identity of central atom of POM clusters varies (H_{8-n}Xⁿ⁺W₁₂O₄₀, Xⁿ⁺ = P⁵⁺, Si⁴⁺, Al³⁺, or Co²⁺), as plotted in Figure 4a,b as open symbols with their regressed dotted lines. In combine with eqs 5e and 6a as well as eq 8a,b, these dotted lines correlate k_{mono} and k_{dimer} to DPE, as captured in the following relations:

$$ln(k_{mono}, \frac{10^{-3} \, \mu mol}{\mu mol_{H^{+}} \, kPa \, s}) = -\frac{(1 - \alpha_{mono}T) \Delta H_{mono}^{\ddagger}}{RT} + ln(A_{mono})$$

$$= -\frac{(1 - \alpha_{mono}T) \chi_{mono}DPE}{RT} + ln\left(A_{mono}e^{-\frac{(1 - \alpha_{mono}T) \psi_{mono}}{RT}}\right)$$

$$= -0.094 \left(\frac{mol}{kJ}\right) DPE \left(\frac{kJ}{mol}\right) + ln\left(e^{109}, \frac{10^{-3} \, \mu mol}{\mu mol_{H^{+}} \, kPa \, s}\right)$$

$$ln(k_{dimer}, \frac{10^{-3} \, \mu mol}{\mu mol_{H^{+}} \, s}) = -\frac{(1 - \alpha_{dimer}T) \Delta H_{dimer}^{\ddagger}}{RT} + ln(A_{dimer})$$

$$= -\frac{(1 - \alpha_{dimer}T) \chi_{dimer}DPE}{RT} + ln\left(A_{dimer}e^{-\frac{(1 - \alpha_{dimer}T) \psi_{dimer}}{RT}}\right)$$

$$= -0.042 \left(\frac{mol}{kJ}\right) DPE \left(\frac{kJ}{mol}\right) + ln\left(e^{49.8}, \frac{10^{-3} \, \mu mol}{\mu mol_{H^{+}} \, s}\right)$$
(9b)

The terms of $ln(e^{109}, 10^{-3} \, \mu\text{mol} \, (\mu\text{mol}_{\text{H}^+} \, \text{kPa s})^{-1})$ and $ln(e^{49.8}, 10^{-3} \, \mu\text{mol} \, (\mu\text{mol}_{\text{H}^+} \, \text{s})^{-1})$ are constants that capture the contributions coming from all the other terms in eqs 5d,f, 6b, 8a,b, except for the DPE.

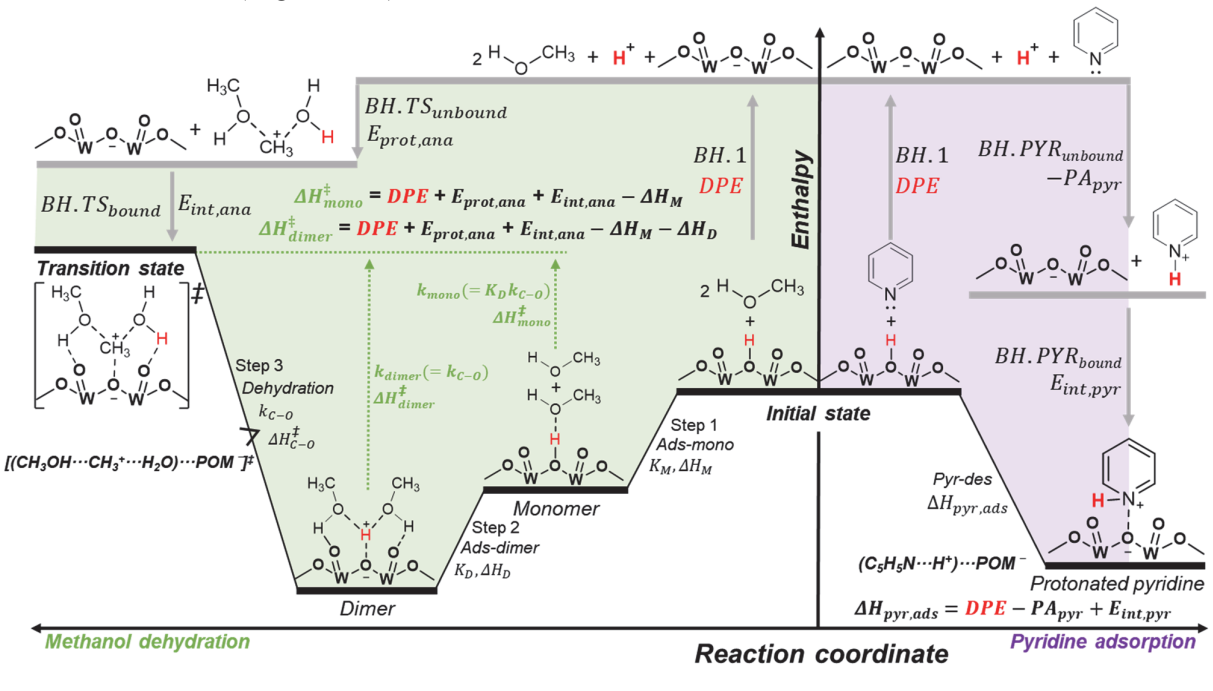
At 433 K, the calculated $(1 - \alpha_{mono}T)\chi_{mono}$ is 0.34 and $(1 - \alpha_{dimer}T)\chi_{dimer}$ is 0.15. We note that $(1 - \alpha_{mono}T)\chi_{mono}$ is larger than $(1 - \alpha_{dimer}T)\chi_{dimer}$ (0.34 vs. 0.15), indicating that k_{mono} is more sensitive to DPE than that of k_{dimer} (eq 9a,b). This is because the energy cost for deprotonating a proton protonated dimer (DPE) partially compensated during the formation of methanol $((CH_3OH\cdots H^+\cdots CH_3OH)\cdots POM^-)$ and of carbocationic transition state $([(CH_3OH\cdots CH_3^+\cdots H_2O)\cdots POM^-]^{\ddagger}).^{8,18}$ Such correlations (eq 9a,b) have been applied to estimate the DPE of protons on structurally complex, less defined oxides such as SO₄–ZrO₂, WO_x–ZrO₂, and perfluorosulfonic resins catalysts.⁶⁶ Here, we adopt these previously established strategies in (i) exploring the cation effect on Brønsted acid strength modulation on structurally well-defined H_xY_{(4-x)/z}Si clusters with monovalent cations (x = 4-1, $Y^{z+} = Na^+$ or K^+) and (ii) estimating the reactivity-averaged DPE values on structurally more complicated $H_xY_{(4-x)/z}Si$ clusters with di- or tri-valent cations (x = 4-0, $Y^{z+} = Cu^{2+}$, Mg^{2+} , or Al^{3+}), by projecting the measured k_{mono} and k_{dimer} values reported in Figure 2c,d onto the established correlations and back calculating the DPE values from k_{mono} and k_{dimer} ($DPE_{mono,deh}$ and $DPE_{dimer,deh}$, in eq 9a,b, respectively, where the subscript deh denotes the derived DPE values from methanol dehydration reaction), respectively, that are shown in Figure 4a,b. Table S3 of the Supporting Information tabulates the numerical values of $DPE_{mono,deh}$ and $DPE_{dimer,deh}$ for the cluster series. This approach neglects the modulation of acid strength due to methanol adsorption at Brønsted sites, as the increase in DPE values is expected to be comparable across various POM clusters, and it also disregards the modulation caused by methanol adsorption at counter cations, as the expected effect of adsorbed methanol on acid strength modulation of POM clusters is weak compared to that of parent cations.

Figure 4c shows the parity plot between $DPE_{mono,deh}$ and $DPE_{dimer,deh}$. For $H_xY_{(4-x)/z}Si$ clusters with lesser extent of cation exchange (x = 2-4), $DPE_{mono,deh}$ and $DPE_{dimer,deh}$ are consistent with each other. For $H_xY_{(4-x)/z}Si$ clusters with greater extent of cation exchange (x = 0 or 1), the DPE values derived from k_{dimer} become significantly higher than those derived from k_{mono} . We note that k_{dimer} values are less sensitive to DPE⁸ (Figure 4b) and the fact that the saturation of Brønsted sites on POM clusters with protonated dimers (CH₃OH···H⁺····CH₃OH) increases the DPE value because of the injection of charge into the cluster during deprotonation process.⁶ Therefore, the uncertainty of $DPE_{dimer,deh}$ would be larger and $DPE_{mono,deh}$ would be more reliable.

Figure S9a of the Supporting Information illustrates the correlation between $DPE_{mono,deh}$ and $[H^+_{pyr\ TPD-IR}]$ across the $H_xY_{(4-x)/z}Si$ cluster series (x = 4-0, $Y^{z+} = Na^+$, K^+ , Cu^{2+} , Mg^{2+} , or Al^{3+}). For $H_xY_{(4-x)/z}Si$ clusters with monovalent cations ($Y^{z+} = Na^+$ or K^+), their DPE values monotonically increased, ranging from 1100 to 1175 kJ mol⁻¹, as $[H^+_{pyr\ TPD-IR}]$ decreased. Given that all Brønsted sites reside on the surface of these POM clusters (Scheme 1, left), this observation underscores the inhibitory effects of monovalent cations on Brønsted acid strength of remaining protons—the higher extent of cation exchange, the higher DPE values and thus weaker Brønsted acid strength. For $H_xY_{(4-x)/z}Si$ clusters with di- and tri-valent cations ($Y^{z+} = Cu^{2+}$, Mg^{2+} , or Al^{3+}), their DPE values increased, albeit within a smaller DPE range of 1100 to 1150 kJ mol⁻¹, as $[H^+_{pyr\ TPD-IR}]$ decreased. The interpretation of cation effects on Brønsted acid strength modulation on these POM clusters, however, becomes challenging, due to the generation of additional Brønsted sites in the hydroxyl groups associated with these cations on POM clusters, as depicted in Scheme 1 (right). These protons, along with those inherently present on the clusters, contribute to the overall

Brønsted site densities and methanol DEH turnovers. Consequently, the specific impact of these counter cations on the intrinsic Brønsted acid strength of POM is obscured.

Scheme 2. Reaction Coordinates and Born-Haber Thermochemical Analysis for the Evolvement of $[(CH_3OH\cdots CH_3^+\cdots H_2O)\cdots POM^-]^{\ddagger}$ Transition State in Methanol Dehydration to Dimethyl Ether (Left Panel) and for the Formation of Protonated Pyridine $((C_5H_5N\cdots H^+)\cdots POM^-)$ in Pyridine Adsorption at Brønsted Sites on POM Clusters (Right Panel)



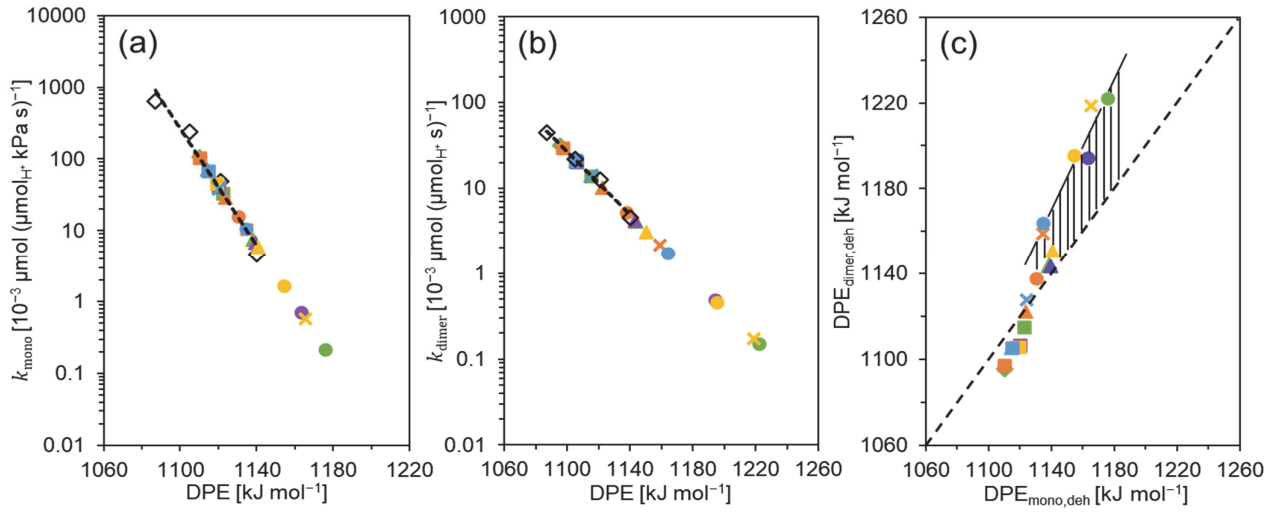


Figure 4. Calibrations of DPE values of Brønsted sites on $H_xY_{(4-x)/z}Si$ cluster series $(x = 4-0, Y^{z+} = Na^+, K^+, Cu^{2+}, Mg^{2+}, or Al^{3+})$ via (a) k_{mono} ($DPE_{mono,deh}$) and (b) k_{dimer} ($DPE_{dimer,deh}$) obtained from data regression shown in Figure S8 of the Supporting Information against eq 4b. (c) Correlations between derived $DPE_{mono,deh}$ and $DPE_{dimer,deh}$ (Green, Na⁺; purple, K⁺; orange, Cu²⁺; gold, Mg²⁺; blue, Al³⁺. Solid diamond, x = 4; solid square, x = 3; solid triangle, x = 2; solid circle, x = 1; cross, x = 0). The reference k_{mono} and k_{dimer} values (open diamond) in (a) and (b) are taken from the literature⁸ on the series of $H_{8-n}X^{n+}W_{12}O_{40}/SiO_2$ clusters ($X^{n+} = P^{5+}$, Si^{4+} , Al^{3+} , or Co^{2+} , n is the valence of central atom X) at the same reaction temperature (433 K). The dashed line in (c) is the parity line.

3.4. Interpretations of Pyridine Temperature Programmed Desorption and Derived DPE Values for $H_xY_{(4-x)/z}Si$ Cluster Series $(x = 4-0, Y^{z+} = Na^+, K^+, Cu^{2+}, Mg^{2+}, or Al^{3+})$

Next, we extract DPE values of the cluster series from pyridine desorption enthalpies ($\Delta H_{pyr,des}$) derived from pyridine-TPD (*Peaks II* and *III*, Figure 1b and Figures S1b–4b of the Supporting Information) with Born-Haber thermochemical analysis, 41,69,70 shown in Scheme 2 (right panel). As shown in the scheme, pyridine (C_5H_5N) interacts with a proton on a POM cluster (H–POM) to form a protonated pyridinium ion (($C_5H_5N\cdots H^+$)····POM⁻), where the proton transfers from the cluster to the N-atom in pyridine, $^{71-73}$ with an adsorption enthalpy $\Delta H_{pyr,ads}$, which equals the negative pyridine desorption enthalpy ($\Delta H_{pyr,ads} = -\Delta H_{pyr,des}$). In analogous to that in methanol dehydration (Scheme 2, left panel), pyridine adsorption at Brønsted sites is decomposed into three fictitious steps of: (i) deprotonation of the Brønsted site (*Step BH.1*) to form a free proton (H⁺) and a conjugate POM⁻ anion (DPE), (ii) protonation of pyridine (*Step BH.PYRunbound*) to form a gaseous pyridinium cation ($C_5H_5N\cdots H^+$) (negative proton affinity of pyridine, $-PA_{pyr} = \sim -940$ kJ mol⁻¹), $^{74-76}$ and (iii) interactions (*Step BH.PYRbound*) between the pyridinium cation and the POM⁻ anion ($E_{int,pyr}$, which equals the sum of electrostatic ($E_{ele,pyr}$) and covalent ($E_{cov,pyr}$) interactions). Closing this Born-Haber cycle, DPE ($DPE_{pyr,TPD}$) equals:

$$DPE_{pyr,TPD} = PA_{pyr} + \Delta H_{pyr,ads} - E_{int,pyr} = PA_{pyr} - \Delta H_{pyr,des} - E_{int,pyr}$$
(10a)

$$E_{int,pyr} = E_{ele,pyr} + E_{cov,pyr}$$
 (10b)

Redhead method derived from the Polanyi-Wigner equation gives the estimated value⁷⁷ of the pyridine desorption enthalpy, $\Delta H_{pyr,des}$, assuming first-order desorption kinetics and a constant pre-exponential factor $(A, 1\times10^{13} \text{ s}^{-1})$ that is independent of pyridine coverage, as a function of the maximum pyridine desorption temperature (T_p) for *Peak III* or *Peak III* (for the case without *Peak III*), and the temperature ramping rate (β) :⁷⁸⁻⁸¹

$$\Delta H_{pyr,des} = RT_p \left[ln \left(\frac{AT_p}{\beta} \right) - 3.46 \right]$$
 (11)

In terms of the interaction energy $E_{int,pyr}$, its value is not available to our best knowledge but can be derived from the reference case of H₄Si cluster with its known DPE value (1105 kJ mol⁻¹)¹⁸ and its derived $\Delta H_{pyr,des}$ from the pyridine-TPD profile (eq 11). Table S4 of the Supporting Information shows calculated $\Delta H_{pyr,des}$, $E_{int,pyr}$, and $DPE_{pyr,TPD}$, based on eqs 10 and 11, by assuming that $E_{int,pyr}$ values for cation exchanged cluster series remain the same with that of unexchanged POM cluster (H₄Si).

Among these derived energies, pyridine desorption enthalpies $\Delta H_{pyr,des}$ for the cluster series are within the range of 198–242 kJ mol⁻¹. These values are in the same order of magnitude with those on Brønsted

acidic zeolites (with DPE values ~1200 kJ mol⁻¹)⁸²—on zeolites, pyridine adsorption enthalpies are ~-200 kJ mol⁻¹ ($\Delta H_{pyr,ads} = -\Delta H_{pyr,des}$) based on microcalorimetry measurements and DFT calculations.^{73,83} Pyridine desorption enthalpies become less positive as DPE values increase (decreasing of nominal H⁺-to-POM ratios) when they are corelated with $DPE_{mono,deh}$, derived from methanol dehydration (Figure S10 of the Supporting Information). Rearranging eq 10a and substituting the term $DPE_{pyr,TPD}$ with $DPE_{mono,deh}$, the intrinsic correlation between $\Delta H_{pyr,des}$ and $DPE_{mono,deh}$ is derived, with a coefficient $\chi_{int,pyr}$ that accounting for the dependence of $E_{int,pyr}$ on DPE:

$$\Delta H_{pyr,des} = PA_{pyr} - (1 + \chi_{int,pyr}) \times DPE_{mono,deh}$$

$$= 940 \text{ kJ mol}^{-1} - (1 + \chi_{int,pyr}) \times DPE_{mono,deh}$$
(12)

Regression of the data shown in Figure S10 of the Supporting Information against eq 12 gives the coefficient $\chi_{int,pyr}$ of -0.37, which coresponds to an interaction energy $(E_{int,pyr})$ ranging between -409 to -435 kJ mol⁻¹ $(E_{int,pyr} = \chi_{int,pyr}DPE_{mono,deh})$. Our assumption underestimates the $E_{int,pyr}$ value (less negative, constant -407 kJ mol⁻¹) and thus overestimates the Brønsted acid strength (smaller DPE values) of cation exchanged POM clusters. The more negative $E_{int,pyr}$ values stem from the more effective electrostatic stabilization of pyridinium cation on the POM⁻ anion with higher DPE values (more negative $E_{ele,pyr}$, relatively stable $E_{cov,pyr}$, eq 10b), as we derived from the similar interactions between a protonated methanol dimer (CH₃OH···H⁺····CH₃OH) and the POM⁻ anion on the series of POM clusters with different DPE values (1068-1142 kJ mol⁻¹, 188-100 kJ mol

Figure 5 shows the parity plot for $DPE_{pyr,TPD}$ derived from pyridine-TPD and $DPE_{mono,deh}$ from methanol dehydration. For $H_xY_{(4-x)/z}Si$ clusters with lesser extent of cation exchange (x = 2-4), these DPE values are well correlated with each other, in agreement with the trend derived from the first- and zero-order rate constants in methanol dehydration $(DPE_{mono,deh} \text{ vs. } DPE_{dimer,deh})$ shown in Figure 4c. For $H_xY_{(4-x)/z}Si$ clusters with greater extent of cation exchange (x = 0 or 1), $DPE_{pyr,TPD}$ values deviate from $DPE_{mono,deh}$ values. This discrepancy likely arises from the underestimated $DPE_{pyr,TPD}$ values (~30 kJ mol⁻¹ lower, overestimated Brønsted acid strength) on POM clusters with weaker Brønsted acid strength caused by the assumption of constant $E_{int,pyr}$ used in eq 10a. Consequently, the $DPE_{pyr,TPD}$ values vary within a narrower range of 1100 to 1150 kJ mol⁻¹ across the $H_xY_{(4-x)/z}Si$ cluster series $(x = 4-0, Y^{z+} = Na^+, K^+, Cu^{2+}, Mg^{2+}, or$

Al³⁺), correlating with the decrease in Brønsted site densities of $[H_{pyr\,TPD-IR}^+]$, as depicted in Figure S9b of the Supporting Information.

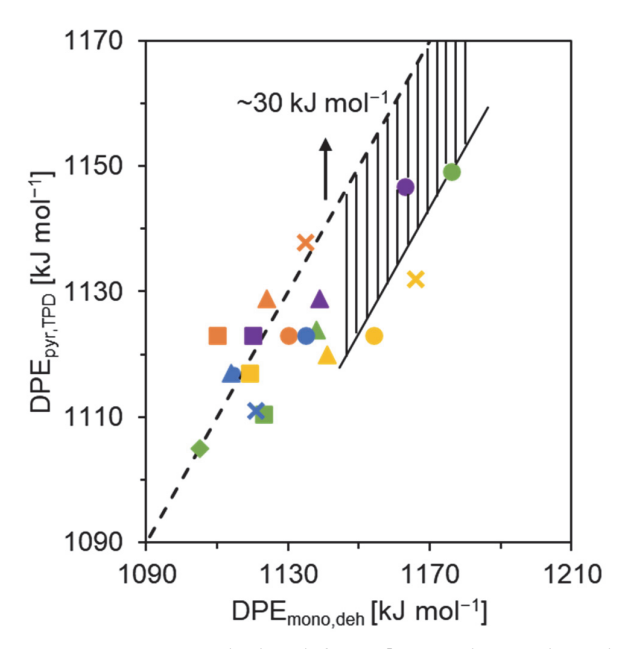
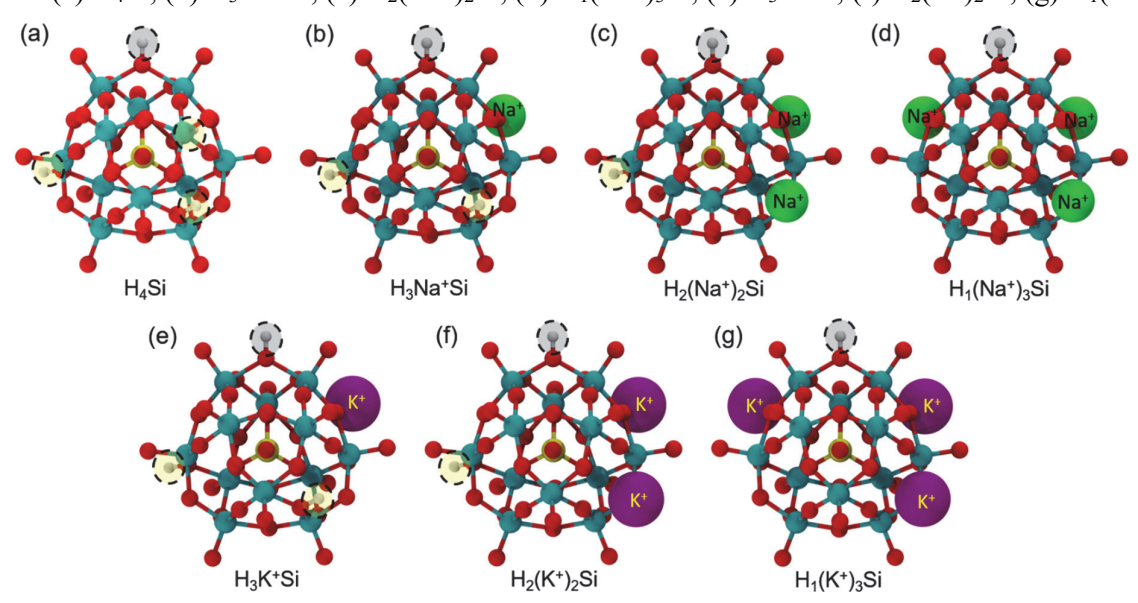


Figure 5. Correlations between $DPE_{mono,deh}$ derived from k_{mono} in methanol dehydration and $DPE_{pyr,TPD}$ derived from pyridine-TPD studies over $H_xY_{(4-x)/z}Si$ cluster series (x = 4-0, $Y^{z+} = Na^+$ (green), K^+ (purple), Cu^{2+} (orange), Mg^{2+} (gold), or Al^{3+} (blue). Diamond, x = 4; square, x = 3; triangle, x = 2; circle, x = 1; cross, x = 0). The dashed line represents the parity line, while the solid line indicates the trend of the data points deviating from it.

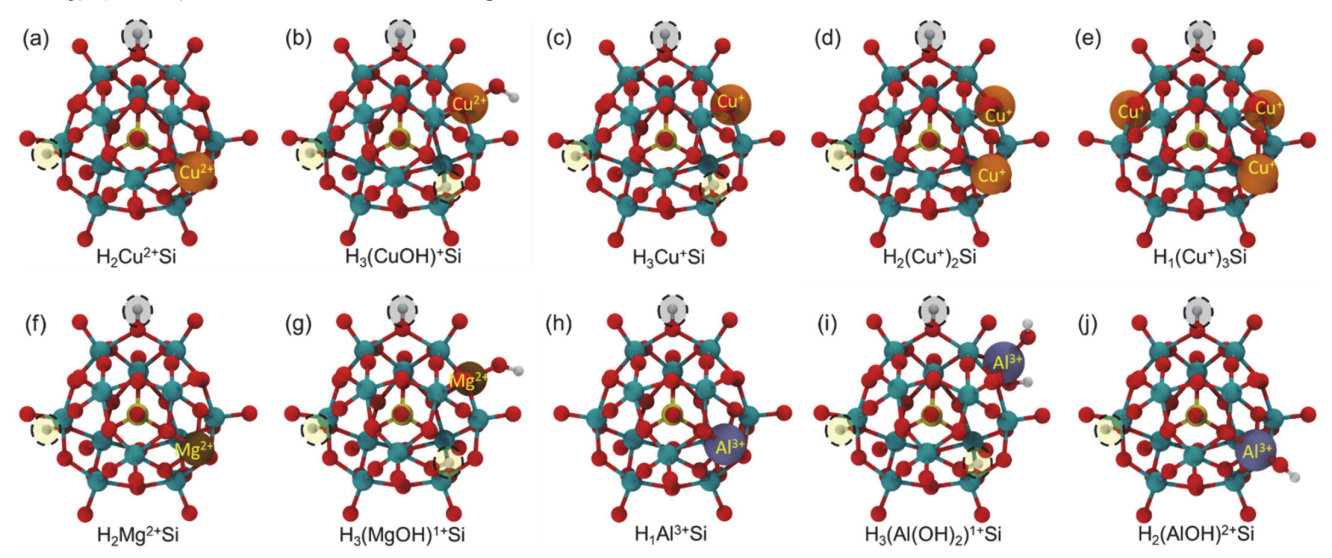
3.5. Origins of DPE Modulations upon Cation Exchanges on H₄Si POM Clusters

Scheme 3. Structures of Investigated Unexchanged and Monovalent Cations (Na⁺ or K⁺) Exchanged H₄Si Clusters of (a) H₄Si, (b) H₃Na⁺Si, (c) H₂(Na⁺)₂Si, (d) H₁(Na⁺)₃Si, (e) H₃K⁺Si, (f) H₂(K⁺)₂Si, (g) H₁(K⁺)₃Si



White: H, red: O, dark yellow: Si, dark teal: W. Note: DPE is calculated by removing the proton within the grey circle.

Scheme 4. Locations of (a) Cu^{2+} , (b) $(CuOH)^+$, (c)–(e) Cu^+ , (f) Mg^{2+} , (g) $(MgOH)^+$, (h) Al^{3+} , (i) $(Al(OH)_2)^+$, and (j) $(AlOH)^{2+}$ Cations on the Investigated H₄Si Clusters



White: H, red: O, dark yellow: Si, dark teal: W. Note: DPE is calculated by removing the proton within the grey circle.

DFT calculations provide the DPE values ($DPE = E_{POM^-} + E_{H^+} - E_{POM}$) of POM clusters and their modulation, after exchanging a portion of protons with cations of different chemical identities and valences. Schemes 3 and 4 show structures of unexchanged and cation exchanged POM clusters used for DPE calculations. In each case, the DPE is calculated by removing the top-most proton (within the grey circle) shown in the structure, while other protons are exchanged to determine the effect of vicinal counter cations on the DPE of the same proton. We note that, when dispersion these clusters on silica, the DPE values become higher than their bulk, 17,84,85 as previously established through microcalorimetry of NH₃ adsorption/desorption $^{86-88}$ and of pyridine adsorption. 86,89 But at the limit of low surface densities (0.14 POM nm⁻²) used in our studies, DPE values of clusters remain largely independent of their loadings.

DFT calculations were first performed on H₂SW₁₂O₄₀ (H₂SW), H₃PW₁₂O₄₀ (H₃P), and H₄SiW₁₂O₄₀ (H₄Si) clusters with S⁶⁺, P⁵⁺ and Si⁴⁺ central atoms, respectively, using proton locations from previous work based,⁶ in turn, on original location screening by Janik et al.¹⁰ This study, however, utilizes more recent PBE functionals with D3BJ dispersion correction. A comparison between DPE values between previous and this study shows that the current DPE values are on an average of 11 kJ mol⁻¹ higher than a previous work^{6,18} (Table S5 of the Supporting Information), which is consistent with an additional, weak van der Waals interaction between the proton and the anion that must be overcome to remove the proton. The original structure of H₄Si cluster contains one of the four protons bound to a terminal W=O atom of the POM (H₄Si-v1, Figure S11 of the Supporting Information), while all other protons in H₂SW, H₃P and H₄Si POM clusters are bound to W-O-W bridging O-atoms. Cation exchanges were initially performed by replacing protons

with cations at the original proton locations from previous work. The exchange studies revealed, however, that POM clusters were more stable in intact and conjugate anion forms, when Na⁺ cations relaxed into hollow positions within rings formed by W–O–W repeating units, and that four-fold hollow positions were more stable than three-fold hollow positions. Iterations between such location screening and maximization of physical distance between protons and cations in unexchanged and Na⁺ exchanged clusters (Figures S11 and S12 of the Supporting Information), led to the final most stable structures shown in Schemes 3 and 4. The new, more stable proton location found for the unexchanged, intact H₄Si (Scheme 3a and Figure S11 of the Supporting Information, H₄Si-v2) contains the fourth proton at a bridging O-atom near a four-fold hollow instead of a terminal O-atom (W=O). Exchanges of other cations were performed at locations consistent with Na⁺ but the order of proton removal was checked separately for divalent cations to find the most stable location for the exchange.

The optimized H₄Si clusters bearing various types of cations, and the same cation with different valences or hydroxides, i.e., Na⁺, K⁺, Cu²⁺, Cu⁺, (CuOH)⁺, Mg²⁺, (MgOH)⁺, Al³⁺, (AlOH)²⁺, and (Al(OH)₂)⁺), in their most stable configurations were employed to investigate the effect of counter cations on DPE values. Scheme 3b-d illustrates three distinct structures with one, two, or three Na⁺ cations in fourfold hollow sites (H₃Na⁺Si, H₂(Na⁺)₂Si, and H₁(Na⁺)₃Si), while Scheme 3e-g shows the corresponding K⁺ exchanged H₄Si clusters (H₃K⁺Si, H₂(K⁺)₂Si, and H₁(K⁺)₃Si). Scheme 4a-e illustrates five different structures: one with a Cu²⁺ cation (H₂Cu²⁺Si), another with a (CuOH)⁺ cation at a location consistent with the Na⁺ exchanged H₄Si cluster (H₃(CuOH)⁺Si), and the remaining three with one to three Cu⁺ (H₃Cu⁺Si, H₂(Cu⁺)₂Si, and H₁(Cu⁺)₃Si). Scheme 4f,g illustrates two nonidentical structures: one with a Mg²⁺ cation at a location consistent with the Cu²⁺ exchanged H₄Si cluster (H₂Mg²⁺Si) and another with a (MgOH)⁺ cation at a location consistent with the Na⁺ exchanged counterpart (H₃(MgOH)¹⁺Si). Scheme 4h-j captures three dissimilar structures: one with a Al³⁺ cation (H₁Al³⁺Si), another with a (Al(OH)₂)¹⁺ cation at a location consistent with the Na⁺ exchanged H₄Si cluster (H₃Al(OH)₂)¹⁺Si), and a third with a (AlOH)²⁺ cation at a location consistent with the Cu²⁺ exchanged H₄Si-re cluster (H₂(AlOH)²⁺Si). In these calculations, we ignore the modulation of Brønsted acid strength arising from methanol adsorption at counter cations, as the expected effect of adsorbed methanol on the acid strength of POM clusters is weak compared to that of parent counter cations.⁶

Figure 6a compares DPE values obtained from DFT calculations (DPE_{DFT}) for the investigated POM structures shown in Schemes 3 and 4 with those derived from methanol dehydration rate measurements ($DPE'_{mono,deh}$) on $H_xY_{(4-x)/z}Si$ clusters (x = 4-1, $Y^{z+} = Na^+$, K^+ , Cu^{2+} , Mg^{2+} , and Al^{3+}) adjusted for DFT-related discrepancies ($DPE'_{mono,deh} = DPE_{mono,deh} + 11 \text{ kJ mol}^{-1}$). For monovalent cation exchanged $H_xY_{(4-x)/z}Si$

 x_1/z_2 Si clusters (x = 3-1, $Y^{z^+} = Na^+$ or K^+), theoretical calculations align well with experimental derived results. The calculated DPE values increase from 1116 to 1175 kJ mol⁻¹ as the extent of cation exchange increases and the nominal H⁺-to-POM ratio (x) concomitantly decreases. Comparing Na⁺ and K⁺ cations, K⁺ demonstrates a more pronounced effect on DPE promotion. However, for di- and tri-valent Cu²⁺, Mg²⁺, and Al³⁺ exchanged H_xY_{(4-x)/z}Si clusters, theoretical calculations diverge from experimental observations. The calculated DPE values are smaller than those of unexchanged H₄Si clusters excepting for H₂Mg²⁺Si clusters, while the measured reactivity-averaged DPE values are slightly higher because of the interference caused by the weak Brønsted acid sites associated with hydroxides. For these di- and tri-valent cations, we also consider the more reduced Cu⁺ cation⁵⁷ and their associated hydroxides ((CuOH)⁺, (MgOH)⁺, (AlOH)²⁺, (Al(OH)₂)¹⁺, structures shown in Scheme 4), all exhibiting an inhibitory effect on DPE of remaining protons on POM clusters, excepting for H₃Cu⁺Si and H₂(Cu⁺)₂Si clusters, which show a slight promotion effect on DPE.

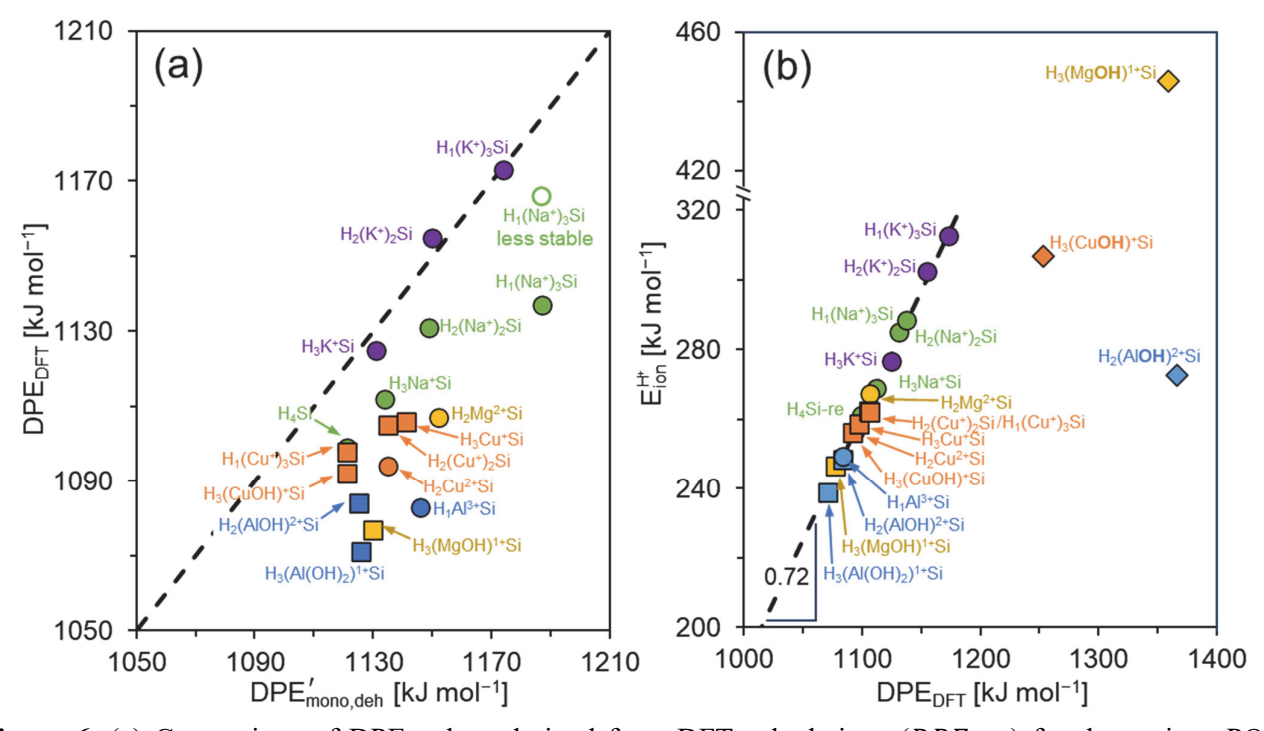


Figure 6. (a) Comparison of DPE values derived from DFT calculations (DPE_{DFT}) for the various POM structures shown in Schemes 3 and 4 and those derived from kinetic assessments with methanol dehydration chemistry ($DPE'_{mono,deh}$) on $H_xY_{(4-x)/z}Si$ clusters (x = 4-0, $Y^{z+} = Na^+$, K^+ , Cu^{2+} , Mg^{2+} , and Al^{3+}) after considering the discrepancy in DPE values stemming from DFT calculations between this work and prior research ($DPE'_{mono,deh} = DPE_{mono,deh} + 11 \text{ kJ mol}^{-1}$). The dashed line is the parity line. (b) Ionic components of DPE (E_{ion}^{H+} , $DPE = E_{ion}^{H+} + E_{cov}^{H+}$) for the various POM structures and the associated hydroxyl groups in $CuOH^+$, $MgOH^+$, and $AlOH^{2+}$ cations, plotted as a function of their DPE_{DFT} values. The dashed line represents the linear regression of these data points, excluding those from hydroxides.

previously established from examining the potential energy profiles for heterolytic O-H bond dissociation, 90 and from theoretical analyses of molecular orbital hybridization. For Keggin-type POM clusters, $E_{ion}^{H^+}$ reflects the electrostatic forces between the charge balancing proton and the conjugate POM⁻ anion, ⁶ while $E_{cov}^{H^+}$ signifies the stabilization of the ion pair through electronic and structural reorganizations, as well as the electron sharing among neighboring ions. 92,93 Table S6 of the Supporting Information summarizes $E_{ion}^{H^+}$ and $E_{cov}^{H^+}$ for the investigated POM clusters shown in Schemes 3 and 4 and for the associated hydroxyl groups in the $(CuOH)^+$, $(MgOH)^+$, $(AlOH)^{2+}$ cations, whereas Figure 6b plots these $E_{ion}^{H^+}$ values as a function of their DPE values. Although $E_{ion}^{H^+}$ (239–446 kJ mol⁻¹, Table S6 of the Supporting Information) is much smaller than $E_{cov}^{H^+}$ (831–1093 kJ mol⁻¹)—proportionality factor for the ionic interactions, $dE_{ion}^{H^+}/d(DPE)$, is 0.72 (Figure 6b), whereas that for the covalent interactions, $dE_{cov}^{H^+}/d(DPE)$, is much smaller at 0.28. This finding aligns with previously reported data on $H_{8-n}X^{n+}W_{12}O_{40}$ clusters $(X^{n+} = S^{6+}, P^{5+}, Si^{4+}, Al^{3+}, Co^{2+}; P^{5+}, Si^{4+}, Al^{5+}, Co^{5+}; P^{5+}, Si^{5+}, R^{5+}, R^{5+}$ $dE_{ion}^{H^+}/d(DPE) = 0.75\pm0.08$ and $dE_{cov}^{H^+}/d(DPE) = 0.25\pm0.08)^6$ and underscores the primary effect of counter cations on the ionic vs. the covalent component. For protons in the investigated hydroxides, their DPE values (1253-1366 kJ mol⁻¹, Table S6 of the Supporting Information) exceed those of protons on POM clusters and their associated $E_{ion}^{H^+}$ diverges from the established trend. Taken together, these results confirm that protons associated with hydroxides exhibit weak Brønsted acid strength due to their unique electronic characteristics arising from distinct structural features.⁹⁴

Previous studies showed that changes in the ionic component of DPE $(E_{ion}^{H^+})$ arising from changing central atom of POM clusters are correlated with the Bader charges on the $X^{n+}O_4^{4-}$ tetrahedral core $(q_{X^{n+}O_4^{4-}}^{neutral})$ at the center of the neutral Keggin clusters.⁶ Specifically, central cations with lower valence exhibited a more negative charge on the central tetrahedron, which increased the ionic component, because the proton needs to overcome a greater electrostatic interaction to achieve deprotonation.⁹⁵ Here, we evaluate if the current changes in $E_{ion}^{H^+}$ imposed by exchanging surface protons with counter cations is also due to changes in the charge on the central SiO_4^{4-} tetrahedra. The calculated Bader charges in $q_{SiO_4^{4-}}^{neutral}$ remain constant at ~3.13 e across all investigated POM structures, shown in Table S6 of the Supporting Information. These results indicate that cation exchange has virtually no effect on the central tetrahedron charge. Instead, the electron density injected into the POM clusters remains in the W₁₂O₃₆ oxide shell. Yet,

the proton must overcome the electrostatic interaction due to this additional negative charge, which increases the DPE.

The charge distribution within the $W_{12}O_{36}$ oxide shell correlates with the atomic electronegativity of investigated counter cations (χ) , 15,37 which is the arithmetic mean of their ionization energy (I) and electron affinity (A), $\chi = (I + A)/2$. $^{96-98}$ For the series of cations investigated here, their atomic electronegativities increase from ~2.5 eV for K-atom (2.42 eV) and Na-atom (2.85 eV) to ~4.5 eV for Al-atom (3.23 eV), Mg-atom (3.75 eV), and Cu-atom (4.48 eV). 99 Therefore, POM clusters containing Na⁺ and K⁺ cations exhibit greater charge localization within the $W_{12}O_{36}$ shell, compared to those containing Cu⁺, Cu²⁺, Mg²⁺, and Al³⁺ cations, thereby resulting in higher anticipated DPE values.

4. CONCLUSIONS

We establish the effects of counter cations, in terms of their chemical identity, valence, and surface density, on modulating the Brønsted acid strength of remaining protons on Keggin-type polyoxometalate tungstosilicic acid clusters (H₄SiW₁₂O₄₀) with methanol dehydration kinetic and pyridine temperature programmed desorption probes. For monovalent cation exchanged $H_x Y_{(4-x)/z} Si$ clusters $(Y^{z+} = Na^+ \text{ or } K^+)$, the DPE values of the remaining protons on POM clusters increase from 1100 to 1175 kJ mol⁻¹ with decreasing nominal H⁺-to-POM ratios. For di- and tri-valent cation exchanged $H_x Y_{(4-x)/z} Si$ clusters $(Y^{z+} = Cu^{2+}, Mg^{2+}, or$ Al³⁺), these cations exchange with protons as cation-hydroxides, with a portion dispersing on the silica support, thereby creating Lewis acid and weak Brønsted acid sites. The overall DPE values of the residual protons on these POM clusters fall in the range of 1100 to 1150 kJ mol⁻¹. Density functional theory calculations demonstrate that counter cations influence the charge distributions within the W₁₂O₃₆ oxide shell without disrupting the charge on the central SiO₄⁴⁻ tetrahedral core, thereby affecting the ionic component of DPE more than its covalent counterpart. The lower atomic electronegativity of monovalent cations, which results in greater electron donation to the oxide shell, is the primary electronic property contributing to higher DPE values on POM clusters compared to di- and tri-valent cations. This work broadens the design and library of Brønsted acidic catalysts with diverse acidities and densities of unconfined protons and aids in the elucidation of site electrostatic correlations on structurally constrained catalysts.

AUTHOR INFORMATION

Corresponding Authors

Prashant Deshlahra – Department of Chemical and Biological Engineering, Tufts University, Medford, Massachusetts 02155, United States; orcid.org/0000-0002-1063-4379; Email: Prashant.Deshlahra@tufts.edu

Ya-Huei (Cathy) Chin – Department of Chemical Engineering and Applied Chemistry, University of Toronto, Toronto, Ontario M5S 3E5, Canada; orcid.org/0000-0003-4388-0389; Phone: +1 (416) 978-8868; Email: cathy.chin@utoronto.ca; Fax: +1 (416) 978-8605

Author

Guangming Cai – Department of Chemical Engineering and Applied Chemistry, University of Toronto, Toronto, Ontario M5S 3E5, Canada; orcid.org/0009-0006-5799-6445

ASSOCIATED CONTENT

Supporting Information

Summary of pyridine-TPD profiles, peak deconvolution, pyridine-IR spectra, and the associated Brønsted and Lewis site densities over the investigated POM clusters and reference samples; assessment of methanol DEH turnover rates at Brønsted and Lewis acid sites; kinetic studies and the rate equation derivation of methanol DEH turnovers; summary of kinetic parameters and calibrated DPE values; DFT calculations of DPE values on various investigated POM structures (PDF)

ACKNOWLEDGEMENTS

This study was financially supported by Suncor Energy Inc. and Natural Sciences and Engineering Research Council of Canada (NSERC) through Collaborative Research and Development Grant CRDPJ543577-19. P.D. acknowledges support from US National Science Foundation (NSF award 2045675) and computational resources from Advanced Cyberinfrastructure Coordination Ecosystem: Services & Support (ACCESS, allocation CTS150005, supported by NSF award 2137603). G.C. acknowledges Hatch Graduate Scholarship for Sustainable Energy Research, Climate Positive Energy Graduate Scholarship, and Bert Wasmund Graduate Fellowship in Sustainable Energy Research for support. We appreciate helpful discussions with Dr. Zhi Wen Chen (University of Toronto) on DFT calculations.

REFERENCES

- (1) Pope, M. T.; Müller, A. Polyoxometalate Chemistry: An Old Field with New Dimensions in Several Disciplines. *Angew. Chemie Int. Ed. English* **1991**, *30*, 34–48.
- (2) Long, D.-L.; Burkholder, E.; Cronin, L. Polyoxometalate Clusters, Nanostructures and Materials: From Self Assembly to Designer Materials and Devices. *Chem. Soc. Rev.* **2007**, *36*, 105–121.
- (3) Barteau, M. A.; Lyons, J. E.; Song, I. K. Surface Chemistry and Catalysis on Well-Defined Oxide Surfaces: Nanoscale Design Bases for Single-Site Heterogeneous Catalysts. *J. Catal.* **2003**, *216*, 236–245.
- (4) Lian, L.; Zhang, H.; An, S.; Chen, W.; Song, Y.-F. Polyoxometalates-Based Heterogeneous Catalysts in Acid Catalysis. *Sci. China Chem.* **2021**, *64*, 1117–1130.
- (5) Kozhevnikov, I. V. Heteropoly Acids and Related Compounds as Catalysts for Fine Chemical

- Synthesis. Catal. Rev. 1995, 37, 311–352.
- (6) Deshlahra, P.; Carr, R. T.; Iglesia, E. Ionic and Covalent Stabilization of Intermediates and Transition States in Catalysis by Solid Acids. *J. Am. Chem. Soc.* **2014**, *136*, 15229–15247.
- (7) Macht, J.; Janik, M. J.; Neurock, M.; Iglesia, E. Mechanistic Consequences of Composition in Acid Catalysis by Polyoxometalate Keggin Clusters. *J. Am. Chem. Soc.* **2008**, *130*, 10369–10379.
- (8) Carr, R. T.; Neurock, M.; Iglesia, E. Catalytic Consequences of Acid Strength in the Conversion of Methanol to Dimethyl Ether. *J. Catal.* **2011**, *278*, 78–93.
- (9) Gounder, R.; Jones, A. J.; Carr, R. T.; Iglesia, E. Solvation and Acid Strength Effects on Catalysis by Faujasite Zeolites. *J. Catal.* **2012**, *286*, 214–223.
- (10) Janik, M. J.; Macht, J.; Iglesia, E.; Neurock, M. Correlating Acid Properties and Catalytic Function: A First-Principles Analysis of Alcohol Dehydration Pathways on Polyoxometalates. J. Phys. Chem. C 2009, 113, 1872–1885.
- (11) Sarazen, M. L.; Doskocil, E.; Iglesia, E. Catalysis on Solid Acids: Mechanism and Catalyst Descriptors in Oligomerization Reactions of Light Alkenes. *J. Catal.* **2016**, *344*, 553–569.
- (12) Sarazen, M. L.; Iglesia, E. Stability of Bound Species during Alkene Reactions on Solid Acids. *Proc. Natl. Acad. Sci.* **2017**, *114*, 3900–3908.
- (13) Macht, J.; Carr, R. T.; Iglesia, E. Consequences of Acid Strength for Isomerization and Elimination Catalysis on Solid Acids. *J. Am. Chem. Soc.* **2009**, *131*, 6554–6565.
- (14) Knaeble, W.; Carr, R. T.; Iglesia, E. Mechanistic Interpretation of the Effects of Acid Strength on Alkane Isomerization Turnover Rates and Selectivity. *J. Catal.* **2014**, *319*, 283–296.
- (15) Misono, M. Heterogeneous Catalysis by Heteropoly Compounds of Molybdenum and Tungsten. *Catal. Rev. Sci. Eng.* **1987**, *29*, 269–321.
- (16) Bardin, B. B.; Bordawekar, S. V; Neurock, M.; Davis, R. J. Acidity of Keggin-Type Heteropolycompounds Evaluated by Catalytic Probe Reactions, Sorption Microcalorimetry, and Density Functional Quantum Chemical Calculations. *J. Phys. Chem. B* **1998**, *102*, 10817–10825.
- (17) Kozhevnikov, I. V. Catalysis by Heteropoly Acids and Multicomponent Polyoxometalates in Liquid-Phase Reactions. *Chem. Rev.* **1998**, *98*, 171–198.
- (18) Deshlahra, P.; Iglesia, E. Reactivity Descriptors in Acid Catalysis: Acid Strength, Proton Affinity and Host-Guest Interactions. *Chem. Commun* **2020**, *56*, 7371–7398.
- (19) Deshlahra, P.; Iglesia, E. Toward More Complete Descriptors of Reactivity in Catalysis by Solid Acids. *ACS Catal.* **2016**, *6*, 5386–5392.
- (20) Dias, J. A.; Caliman, E.; Dias, S. C. L. Effects of Cesium Ion Exchange on Acidity of 12-Tungstophosphoric Acid. *Microporous Mesoporous Mater.* **2004**, *76*, 221–232.
- (21) Mizuno, N.; Misono, M. Heteropolyacid Catalysts. Curr. Opin. Solid State Mater. Sci. 1997, 2, 84–89.
- (22) Timofeeva, M. N.; Maksimovskaya, R. I.; Paukshtis, E. A.; Kozhevnikov, I. V. Esterification of 2,6-Pyridinedicarboxylic Acid with n-Butanol Catalyzed by Heteropoly Acid H3PW12O40 or Its Ce(III) Salt. *J. Mol. Catal. A. Chem.* **1995**, *102*, 73–77.
- (23) Alharbi, W.; Kozhevnikova, E. F.; Kozhevnikov, I. V. Dehydration of Methanol to Dimethyl Ether over Heteropoly Acid Catalysts: The Relationship between Reaction Rate and Catalyst Acid Strength. *ACS Catal.* **2015**, *5*, 7186–7193.

- (24) da Silva, M. J.; Rodrigues, A. A.; Lopes, N. P. G. Keggin Heteropolyacid Salt Catalysts in Oxidation Reactions: A Review. *Inorganics* **2023**, *11*, 162.
- (25) da Silva, M. J.; Rodrigues, A. A. Metal Silicotungstate Salts as Catalysts in Furfural Oxidation Reactions with Hydrogen Peroxide. *Mol. Catal.* **2020**, *493*, 111104.
- (26) Sun, M.; Zhang, J.; Putaj, P.; Caps, V.; Lefebvre, F.; Pelletier, J.; Basset, J. M. Catalytic Oxidation of Light Alkanes (C1-C4) by Heteropoly Compounds. *Chem. Rev.* **2014**, *114*, 981–1019.
- (27) Highfield, J. G.; Moffat, J. B. Characterization of 12-Tungstophosphoric Acid and Related Salts Using Photoacoustic Spectroscopy in the Infrared Region I. Thermal Stability and Interactions with Ammonia. *J. Catal.* **1984**, *88*, 177–187.
- (28) Highfield, J. G.; Moffat, J. B. Characterization of 12-Tungstophosphoric Acid and Related Salts Using Photoacoustic Spectroscopy in the Infrared Region II. Interactions with Pyridine. *J. Catal.* **1984**, *89*, 185–195.
- (29) Narasimharao, K.; Brown, D. R.; Lee, A. F.; Newman, A. D.; Siril, P. F.; Tavener, S. J.; Wilson, K. Structure-Activity Relations in Cs-Doped Heteropolyacid Catalysts for Biodiesel Production. *J. Catal.* **2007**, *248*, 226–234.
- (30) Wilke, T. J.; Barteau, M. A. Cation Exchange Effects on Methanol Oxidation and Dehydration by Supported Polyoxometalates. *J. Catal.* **2019**, *371*, 357–367.
- (31) Wilke, T.; Barteau, M. A. Dehydration and Oxidation of Alcohols by Supported Polyoxometalates: Effects of Mono- and Multivalent Cation Exchange on Catalyst Acidity and Activity. *Ind. Eng. Chem. Res.* **2019**, *58*, 14752–14760.
- (32) Noda, T.; Suzuki, K.; Katada, N.; Niwa, M. Combined Study of IRMS-TPD Measurement and DFT Calculation on Brønsted Acidity and Catalytic Cracking Activity of Cation-Exchanged Y Zeolites. *J. Catal.* **2008**, *259*, 203–210.
- (33) Suzuki, K.; Noda, T.; Sastre, G.; Katada, N.; Niwa, M. Periodic Density Functional Calculation on the Brønsted Acidity of Modified Y-Type Zeolite. *J. Phys. Chem. C* **2009**, *113*, 5672–5680.
- (34) Wu, W.; Weitz, E. Modification of Acid Sites in ZSM-5 by Ion-Exchange: An in-Situ FTIR Study. *Appl. Surf. Sci.* **2014**, *316*, 405–415.
- (35) Celik, F. E.; Kim, T. J.; Bell, A. T. Effect of Zeolite Framework Type and Si/Al Ratio on Dimethoxymethane Carbonylation. *J. Catal.* **2010**, *270*, 185–195.
- (36) Yang, Y.; Lin, F.; Tran, H.; Chin, Y. H. C. Butanal Condensation Chemistry Catalyzed by Brønsted Acid Sites on Polyoxometalate Clusters. *ChemCatChem* **2017**, *9*, 287–299.
- (37) Ghosh, A. K.; Moffat, J. B. Acidity of Heteropoly Compounds. J. Catal. 1986, 101, 238–245.
- (38) Cai, G.; Chin, Y. C. Catalytic Consequences of Protons in Methanol Oxidative Dehydrogenation on Molybdenum-Based Polyoxometalate Clusters. *ACS Catal.* **2024**, *14*, 6674–6686.
- (39) Nie, H.; Howe, J. Y.; Lachkov, P. T.; Chin, Y. H. C. Chemical and Structural Dynamics of Nanostructures in Bimetallic Pt-Pd Catalysts, Their Inhomogeneity, and Their Roles in Methane Oxidation. *ACS Catal.* **2019**, *9*, 5445–5461.
- (40) Cai, G.; Chin, Y. C. Catalytic Sequences and Kinetic Requirements for C-O Bond Scission and Formation in Methanol and Trioxane on Solid Polyoxometalate Clusters. *ACS Catal.* **2023**, *13*, 14828–14844.

- (41) Broomhead, W. T.; Chin, Y. C. Functional Assessment of the Lewis Acid Strength of Structurally Complex Solid Acids. *ACS Catal.* **2024**, *14*, 2235–2245.
- (42) Zheng, S.; Heydenrych, H. R.; Jentys, A.; Lercher, J. A. Influence of Surface Modification on the Acid Site Distribution of HZSM-5. *J. Phys. Chem. B* **2002**, *106*, 9552–9558.
- (43) Kresse, G.; Furthmüller, J. Efficiency of Ab-Initio Total Energy Calculations for Metals and Semiconductors Using a Plane-Wave Basis Set. *Comput. Mater. Sci.* **1996**, *6*, 15–50.
- (44) Kresse, G.; Hafner, J. Ab Initio Molecular Dynamics for Liquid Metals. *Phys. Rev. B* **1993**, *47*, 558–561.
- (45) Perdew, J. P.; Burke, K.; Ernzerhof, M. Generalized Gradient Approximation Made Simple. *Phys. Rev. Lett.* **1996**, 77, 3865–3868.
- (46) Grimme, S.; Ehrlich, S.; Goerigk, L. Effect of the Damping Function in Dispersion Corrected Density Functional Theory. *J. Comput. Chem.* **2011**, *32*, 1456–1465.
- (47) Blöchl, P. E. Projector Augmented-Wave Method. *Phys. Rev. B* **1994**, *50*, 17953–17979.
- (48) Pack, J. D.; Monkhorst, H. J. Special Points for Brillouin-Zone Integrations. *Phys. Rev. B* **1976**, *13*, 5188–5192.
- (49) Makov, G.; Payne, M. C. Periodic Boundary Conditions in Ab Initio Calculations. *Phys. Rev. B* **1995**, 51, 4014–4022.
- (50) Izumi, Y.; Hasebe, R.; Urabe, K. Catalysis by Heterogeneous Supported Heteropoly Acid. *J. Catal.* **1983**, *84*, 402–409.
- (51) Madhusudhan Rao, P.; Wolfson, A.; Kababya, S.; Vega, S.; Landau, M. V. Immobilization of Molecular H3PW12O40 Heteropolyacid Catalyst in Alumina-Grafted Silica-Gel and Mesostructured SBA-15 Silica Matrices. J. Catal. 2005, 232, 210–225.
- (52) Deshlahra, P.; Carr, R. T.; Chai, S. H.; Iglesia, E. Mechanistic Details and Reactivity Descriptors in Oxidation and Acid Catalysis of Methanol. *ACS Catal.* **2015**, *5*, 666–682.
- (53) Lin, F.; Chin, Y. H. C. Catalytic Pathways and Kinetic Requirements for Alkanal Deoxygenation on Solid Tungstosilicic Acid Clusters. *ACS Catal.* **2016**, *6*, 6634–6650.
- (54) Emeis, C. A. Determination of Integrated Molar Extinction Coefficients for Infrared Absorption Bands of Pyridine Adsorbed on Solid Acid Catalysts. *J. Catal.* **1993**, *141*, 347–354.
- (55) Saito, Y.; Cook, P. N.; Niiyama, H.; Echigoya, E. Dehydration of Alcohols on/in Heteropoly Compounds. *J. Catal.* **1985**, *95*, 49–56.
- (56) Okuhara, T.; Mizuno, N.; Misono, M. Catalytic Chemistry of Heteropoly Compounds. *Adv. Catal.* **1996**, *41*, 113–252.
- (57) Baba, T.; Watanabe, H.; Ono, Y. Generation of Acidic Sites in Metal Salts of Heteropolyacids. *J. Phys. Chem.* **1983**, *87*, 2406–2411.
- (58) Mizuno, N.; Misono, M. Heteropolyanions in Catalysis. J. Mol. Catal. 1994, 86, 319–342.
- (59) Baertsch, C. D.; Komala, K. T.; Chua, Y. H.; Iglesia, E. Genesis of Brønsted Acid Sites during Dehydration of 2-Butanol on Tungsten Oxide Catalysts. *J. Catal.* **2002**, *205*, 44–57.
- (60) Di Iorio, J. R.; Hoffman, A. J.; Nimlos, C. T.; Nystrom, S.; Hibbitts, D.; Gounder, R. Mechanistic Origins of the High-Pressure Inhibition of Methanol Dehydration Rates in Small-Pore Acidic Zeolites.

- *J. Catal.* **2019**, *380*, 161–177.
- (61) Cai, G.; Broomhead, W. T.; Chin, Y. H. C.; Cai, H. Advanced Kinetic and Titration Strategies for Assessing the Intrinsic Kinetics on Oxide and Sulfide Catalysts. *Top. Catal.* **2023**, *66*, 1102–1119.
- (62) Yao, R.; Herrera, J. E.; Chen, L.; Chin, Y. H. C. Generalized Mechanistic Framework for Ethane Dehydrogenation and Oxidative Dehydrogenation on Molybdenum Oxide Catalysts. ACS Catal. 2020, 10, 6952–6968.
- (63) Bond, G. C.; Keane, M. A.; Kral, H.; Lercher, J. A. Compensation Phenomena in Heterogeneous Catalysis: General Principles and a Possible Explanation. *Catal. Rev. Sci. Eng.* **2000**, *42*, 323–383.
- (64) Liu, L.; Guo, Q.-X. Isokinetic Relationship, Isoequilibrium Relationship, and Enthalpy–Entropy Compensation. *Chem. Rev.* **2001**, *101*, 673–695.
- (65) Gounder, R.; Iglesia, E. The Catalytic Diversity of Zeolites: Confinement and Solvation Effects within Voids of Molecular Dimensions. *Chem. Commun* **2013**, *49*, 3491–3509.
- (66) Macht, J.; Carr, R. T.; Iglesia, E. Functional Assessment of the Strength of Solid Acid Catalysts. *J. Catal.* **2009**, *264*, 54–66.
- (67) Misono, M. Catalysis of Heteropoly Compounds (Polyoxometalates). In *Studies in Surface Science* and Catalysis; 2013; Vol. 176, pp 97–155.
- (68) Okuhara, T.; Kasai, A.; Hayakawa, N.; Yoneda, Y.; Misono, M. Catalysis by Heteropoly Compounds. VI. The Role of the Bulk Acid Sites in Catalytic Reactions over NaxH3-XPW12O40. *J. Catal.* **1983**, 83, 121–130.
- (69) Lee, C.; Parrillo, D. J.; Gorte, R. J.; Farneth, W. E. Relationship between Differential Heats of Adsorption and Bronsted Acid Strengths of Acidic Zeolites: H-ZSM-5 and H-Mordenite. *J. Am. Chem. Soc.* **1996**, *118*, 3262–3268.
- (70) Boronat, M.; Corma, A. What Is Measured When Measuring Acidity in Zeolites with Probe Molecules? *ACS Catal.* **2019**, *9*, 1539–1548.
- (71) Khalil, I.; Celis-Cornejo, C. M.; Thomas, K.; Bazin, P.; Travert, A.; Pérez-Martínez, D. J.; Baldovino-Medrano, V. G.; Paul, J. F.; Maugé, F. In Situ IR-ATR Study of the Interaction of Nitrogen Heteroaromatic Compounds with HY Zeolites: Experimental and Theoretical Approaches. *ChemCatChem* 2020, 12, 1095–1108.
- (72) Castellà-Ventura, M.; Akacem, Y.; Kassab, E.; El Beida, D. Vibrational Analysis of Pyridine Adsorption on the Brønsted Acid Sites of Zeolites Based on Density Functional Cluster Calculations. *J. Phys. Chem. C* **2008**, *112*, 19045–19054.
- (73) Yuan, S.; Shi, W.; Li, B.; Wang, J.; Jiao, H.; Li, Y. W. Theoretical ONIOM2 Study on Pyridine Adsorption in the Channels and Intersection of ZSM-5. *J. Phys. Chem. A* **2005**, *109*, 2594–2601.
- (74) Martin, J. M. L.; François, J. P.; Gijbels, R. Ab Initio Study of the Proton Affinity of a Number of Ortho-substituted Pyridines. *J. Comput. Chem.* **1989**, *10*, 346–357.
- (75) Wind, J. J.; Papp, L.; Happel, M.; Hahn, K.; Andriole, E. J.; Poutsma, J. C. Proton Affinity Of-Oxalylaminoalanine (BOAA): Incorporation of Direct Entropy Correction into the Single-Reference Kinetic Method. *J. Am. Soc. Mass Spectrom.* **2005**, *16*, 1151–1161.
- (76) Aue, D. H.; Webb, H. M.; Bowers, M. T. Proton Affinities, Ionization Potentials, and Hydrogen Affinities of Nitrogen and Oxygen Bases. Hybridization Effects. *J. Am. Chem. Soc.* **1975**, *97*, 4137–4139.

- (77) Redhead, P. A. Thermal Desorption of Gases. *Vacuum* **1962**, *12*, 203–211.
- (78) Ihm, H.; Ajo, H. M.; Gottfried, J. M.; Bera, P.; Campbell, C. T. Calorimetric Measurement of the Heat of Adsorption of Benzene on Pt(111). *J. Phys. Chem. B* **2004**, *108*, 14627–14633.
- (79) Teplyakov, A. V.; Gurevich, A. B.; Yang, M. X.; Bent, B. E.; Chen, J. G. NEXAFS and TPD Studies of Molecular Adsorption of Hydrocarbons on Cu(100): Segmental Correlations with the Heats of Adsorption. *Surf. Sci.* **1998**, *396*, 340–348.
- (80) Ono, L. K.; Cuenya, B. R. Size Effects on the Desorption of O2 from Au2O3/Au0 Nanoparticles Supported on SiO2: A TPD Study. *J. Phys. Chem. C* **2008**, *112*, 18543–18550.
- (81) Vogt, A. D.; Han, T.; Beebe, T. P. Adsorption of 11-Mercaptoundecanoic Acid on Ni(111) and Its Interaction with Probe Molecules. *Langmuir* **1997**, *13*, 3397–3403.
- (82) Jones, A. J.; Iglesia, E. The Strength of Brønsted Acid Sites in Microporous Aluminosilicates. *ACS Catal.* **2015**, *5*, 5741–5755.
- (83) Parrillo, D. J.; Lee, C.; Gorte, R. J.; White, D.; Farneth, W. E. Comparison of the Acidic Properties of H-[Al]ZSM-5, H-[Fe]ZSM-5, and H-[Ga]ZSM-5 Using Microcalorimetry, Hexane Cracking, and Propene Oligomerization. *J. Phys. Chem* **1995**, *99*, 8745–8749.
- (84) Alsalme, A. M.; Wiper, P. V.; Khimyak, Y. Z.; Kozhevnikova, E. F.; Kozhevnikov, I. V. Solid Acid Catalysts Based on H3PW12O40 Heteropoly Acid: Acid and Catalytic Properties at a Gas-Solid Interface. *J. Catal.* **2010**, *276*, 181–189.
- (85) Kamiya, Y.; Okuhara, T.; Misono, M.; Miyaji, A.; Tsuji, K.; Nakajo, T. Catalytic Chemistry of Supported Heteropolyacids and Their Applications as Solid Acids to Industrial Processes. *Catal. Surv. from Asia* **2008**, *12*, 101–113.
- (86) Kozhevnikova, E. F.; Kozhevnikov, I. V. A Calorimetric Study of the Acidity of Bulk and Silica-Supported Heteropoly Acid H3PW12O40. *J. Catal.* **2004**, *224*, 164–169.
- (87) Liu-Cai, F. X.; Sahut, B.; Faydi, E.; Auroux, A.; Hervé, G. Study of the Acidity of Carbon Supported and Unsupported Heteropolyacid Catalysts by Ammonia Sorption Microcalorimetry. *Appl. Catal. A Gen.* **1999**, *185*, 75–83.
- (88) Bardin, B. B.; Davis, R. J. Effect of Water on Silica-Supported Phosphotungstic Acid Catalysts for 1-Butene Double Bond Shift and Alkane Skeletal Isomerization. *Appl. Catal. A Gen.* **2000**, 200, 219–231.
- (89) Dias, J. A.; Caliman, E.; Dias, S. C. L.; Paulo, M.; De Souza, A. T. C. P. Preparation and Characterization of Supported H3PW12O40 on Silica Gel: A Potential Catalyst for Green Chemistry Processes. *Catal. Today* **2003**, *85*, 39–48.
- (90) Kazansky, V. B.; Zelinsky, N. D. The Nature of Adsorbed Carbenium Ions as Active Intermediates in Catalysis by Solid Acids. *Acc. Chem. Res* **1991**, *24*, 379–383.
- (91) Van Santen, R. A.; Kramer, G. J. Reactivity Theory of Zeolitic Brønsted Acidic Sites. *Chem. Rev* **1995**, *95*, 637–660.
- (92) French, S. J. Some Uses of the Polar Molecule Concept in Elementary Chemistry. *J. Chem. Educ.* **1936**, *13*, 122–130.
- (93) Fajans, K. Struktur Und Deformation Der Elektronenhüllen in Ihrer Bedeutung Für Die Chemischen Und Optischen Eigenschaften Anorganischer Verbindungen. *Naturwissenschaften* **1923**, *11*, 165–172.

- (94) Connell, G.; Dumesic, J. A. The Generation of Brønsted and Lewis Acid Sites on the Surface of Silica by Addition of Dopant Cations. *J. Catal.* **1987**, *105*, 285–298.
- (95) Serwicka, E. M.; Bruckman, K.; Haber, J.; Paukshtis, E. A.; Yurchenko, E. N. Acid-Base Properties of H3+nPVnMo12-NO40 Heteropolyacids, Pure and Supported on K3PMo12O40. *Appl. Catal.* **1991**, 73, 153–163.
- (96) Greiner, M. T.; Chai, L.; Helander, M. G.; Tang, W. M.; Lu, Z. H. Transition Metal Oxide Work Functions: The Influence of Cation Oxidation State and Oxygen Vacancies. *Adv. Funct. Mater.* **2012**, 22, 4557–4568.
- (97) Mulliken, R. S. A New Electroaffinity Scale; Together with Data on Valence States and on Valence Ionization Potentials and Electron Affinities. *J. Chem. Phys.* **1934**, *2*, 782–793.
- (98) Mulliken, R. S. Electronic Structures of Molecules XI. Electroaffinity and Molecular Orbitals, Polyatomic Applications. *J. Chem. Phys.* **1935**, *3*, 586–591.
- (99) Pearson, R. G. Absolute Electronegativity and Hardness: Application to Inorganic Chemistry. *Inorg. Chem.* **1988**, *27*, 734–740.